



The Transmission Spectrum of the Potentially Rocky Planet L 98-59 c

Thomas Barclay¹, Kyle B. Sheppard², Natasha Latouf^{1,3}, Avi M. Mandell¹, Elisa V. Quintana¹, Emily A. Gilbert⁴, Giuliano Liuzzi^{1,5}, Geronimo L. Villanueva¹, Giada Arney¹, Jonathan Brande⁶, Knicole D. Colón¹, Giovanni Covone^{7,8}, Ian J. M. Crossfield⁶, Mario Damiano⁴, Shawn D. Domagal-Goldman¹, Thomas J. Fauchez^{1,9}, Stefano Fiscale¹⁰, Francesco Gallo⁷, Christina L. Hedges^{1,11}, Renyu Hu⁴, Edwin S. Kite¹², Daniel Koll¹³, Ravi K. Kopparapu¹, Veselin B. Kostov^{1,14}, Laura Kreidberg¹⁵, Eric D. Lopez¹, James Mang¹⁶, Caroline V. Morley¹⁶, Fergal Mullally¹⁷, Susan E. Mullally¹⁸, Daria Pidhorodetska¹⁹, Joshua E. Schlieder¹, Laura D. Vega^{1,2}, Allison Youngblood¹, and Sebastian Zieba¹⁵

¹ NASA Goddard Space Flight Center, 8800 Greenbelt Road, Greenbelt, MD 20771, USA; thomas.barclay@nasa.gov

² University of Maryland, College Park, MD 20742, USA

³ George Mason University, 4400 University Drive, Fairfax, VA 22030, USA

⁴ Jet Propulsion Laboratory, California Institute of Technology, Pasadena, CA 91109, USA

⁵ University of Basilicata, Via dell'Ateneo Lucano 10, Potenza (PZ), 85100, Italy

⁶ Department of Physics and Astronomy, University of Kansas, 1082 Malott, 1251 Wescoe Hall Drive, Lawrence, KS 66045, USA

⁷ Department of Physics "Ettore Pancini," Università di Napoli Federico II, Napoli, Italy

⁸ INAF, Osservatorio Astronomico di Capodimonte, via Moiariello 16, 80131 Napoli, Italy

⁹ Integrated Space Science and Technology Institute, Department of Physics, American University, Washington, DC 20016, USA

¹⁰ Science and Technology Department, Parthenope University of Naples, CDN IC 4, 80143, Naples, Italy

¹¹ University of Maryland, Baltimore County, 1000 Hilltop Circle, Baltimore, MD 21250, USA

¹² University of Chicago, Chicago, IL 60637, USA

¹³ Peking University, Beijing, People's Republic of China

¹⁴ SETI Institute, 189 Bernardo Ave, Suite 200, Mountain View, CA 94043, USA

¹⁵ Max Planck Institute for Astronomy, Heidelberg, Germany

¹⁶ Department of Astronomy, University of Texas at Austin, Austin, TX 78712, USA

¹⁷ Constellation Energy, 1310 Point Street, Baltimore, MD 21231, USA

¹⁸ Space Telescope Science Institute, 3700 San Martin Drive, Baltimore, MD 21218, USA

¹⁹ Department of Earth and Planetary Sciences, University of California, Riverside, CA 92521, USA

Received 2023 January 25; revised 2024 December 28; accepted 2025 January 3; published 2025 April 2

Abstract

We present observations of the 1.35 ± 0.07 Earth radius planet L 98-59 c, collected using Wide Field Camera 3 on the Hubble Space Telescope (HST). L 98-59 is a nearby (10.6 pc), bright ($H = 7.4$ mag) M3V star that harbors three small, transiting planets. As one of the closest known transiting multi-planet systems, L 98-59 offers one of the best opportunities to probe and compare the atmospheres of rocky planets that formed in the same stellar environment. We measured the transmission spectrum of L 98-59 c, and the extracted spectrum showed marginal evidence (2.1σ) for wavelength-dependent transit depth variations that could indicate the presence of an atmosphere. We forward-modeled possible atmospheric compositions of the planet based on the transmission spectrum. Although L 98-59 was previously thought to be a fairly quiet star, we have seen evidence for stellar activity, and therefore we assessed a scenario where the source of the signal originates with inhomogeneities on the stellar surface. We also see a correlation between transits of L 98-59 c and L 98-59 b collected 12.5 hr apart, which is suggestive (but at $<2\sigma$ confidence) of a contaminating component from the star impacting the exoplanet spectrum. While intriguing, our results are inconclusive and additional data are needed to verify any atmospheric signal. Fortunately, additional data have been collected from both the HST and James Webb Space Telescope. Should this result be confirmed with additional data, L 98-59 c would be the first planet smaller than 2 Earth radii with a detected atmosphere.

Unified Astronomy Thesaurus concepts: Exoplanet atmospheric composition (2021); Super Earths (1655); M dwarf stars (982); Transmission spectroscopy (2133)

1. Introduction

In the post-Kepler era, ground- and space-based transiting exoplanet searches have focused on detecting small planets orbiting small stars (J. A. Burt et al. 2021; O. D. S. Demangeon et al. 2021; E. R. Newton et al. 2021). The primary reason for favoring small stars, mid-M dwarfs and smaller, is that in the near-term they are likely to be the only targets where we might

feasibly detect an atmosphere around a sub-Neptune-sized planet (M. T. Gialluca et al. 2021). Among the first exoplanets to be targeted by the James Webb Space Telescope (JWST) are numerous small planets around cool stars, which will enable us, for the first time, to begin to see the diversity of atmospheres on terrestrial worlds (C. V. Morley et al. 2017; N. E. Batalha et al. 2018, 2023; J. Lustig-Yaeger et al. 2019).

Several small planets orbiting low-mass stars have been observed using the transmission spectroscopy technique with the Hubble Space Telescope (HST). The most prominent of these are the planets that orbit TRAPPIST-1 (J. de Wit et al. 2016, 2018; M. Gillon et al. 2016, 2017; H. R. Wakeford et al. 2019;



Original content from this work may be used under the terms of the [Creative Commons Attribution 4.0 licence](#). Any further distribution of this work must maintain attribution to the author(s) and the title of the work, journal citation and DOI.

L. J. Garcia et al. 2022). While conclusive atmospheric detection has yet to be made for any of the TRAPPIST-1 worlds, these observations have been informative in producing the first limits on atmospheric density and aerosol properties for these planets. For example, HST observations of the TRAPPIST-1 b and c planets (J. de Wit et al. 2016), as well as HST observations of planets d, e, f, and g in this system (J. de Wit et al. 2018), have ruled out a cloud/haze-free, H₂-dominated atmosphere, and have been used to argue that hazy H₂-rich atmospheres could explain the HST data (S. E. Moran et al. 2018). More recently, JWST has observed thermal emission from TRAPPIST-1 b (T. P. Greene et al. 2023) and c (S. Zieba et al. 2023) that suggests these planets likely have thin to no atmospheres.

In addition to TRAPPIST-1, HST observations have enabled us to put constraints on the atmospheric composition of GJ 1214 b (L. Kreidberg et al. 2014), GJ 1132 b (J. E. Libby-Roberts et al. 2021; L. V. Mugnai et al. 2021; M. R. Swain et al. 2021), and HD 97658 b (V. Bourrier et al. 2017; X. Guo et al. 2020), and to measure a low-density atmosphere on K2-18 b (B. Benneke et al. 2019a; A. Tsiaras et al. 2019), TOI-270 d (T. Mikal-Evans et al. 2023), and possibly also 55 Cnc e (A. Tsiaras et al. 2016; V. Bourrier et al. 2018). Additionally, Spitzer was used to demonstrate spectral signatures on the hot Neptune-sized planet LTT 9779 b (I. J. M. Crossfield et al. 2020; D. Dragomir et al. 2020) and rule out a thick atmosphere on LHS 3844 b (L. Kreidberg et al. 2019). Ground-based observations have further constrained the atmospheres of GJ 1132 b, LHS 1140 b, and LTT 1445 Ab (H. Diamond-Lowe et al. 2018, 2020, 2023).

Among the challenges in detecting and characterizing features in the atmospheres of small, rocky worlds with transmission spectroscopy is that spectral features from the star can contaminate those from the planet. Transmission spectroscopy works by taking the difference between the planet's "in-transit" spectrum with the "out-of-transit" spectrum. However, the light source filtering through the planet's atmosphere comes from the transit chord. Stellar heterogeneities (in the form of dark, cool spots and bright, hot faculae) that reside on the stellar disk, but are unocculted by a transiting planet (outside of the transit chord), can dilute or enhance the measured transit depth (P. R. McCullough et al. 2014; B. Rackham et al. 2017; D. Apai et al. 2018; B. V. Rackham et al. 2018, 2019a, 2019b; N. Espinoza et al. 2019; H. R. Wakeford et al. 2019). These errors in transit depth propagate to errors in the planet's spectrum, and can ultimately mask or mimic atmospheric features. While stellar spectral contamination has been identified as problematic for more than a decade (F. Pont et al. 2008, 2013; D. K. Sing et al. 2011; Z. K. Berta et al. 2012; P. R. McCullough et al. 2014; D. Deming & S. Seager 2017), more recent high-precision observations from JWST have shown it to be a limiting factor in confirming the presence of atmospheres on Earth-sized planets (S. E. Moran et al. 2023), including those orbiting TRAPPIST-1 (O. Lim et al. 2023).

Herein, we present HST spectroscopic observations of a potentially rocky planet, L 98-59 c, with a goal of searching for the presence of an atmosphere. This planet was discovered by the Transiting Exoplanet Survey Satellite (TESS), which was designed to discover small planets orbiting bright, nearby stars (G. R. Ricker et al. 2015). A number of TESS discoveries have already been prioritized for JWST observations, and among the most compelling are the planets orbiting L 98-59, a bright

($H = 7.4$ mag), nearby (10.6 pc) M3 dwarf. L 98-59 hosts three transiting planets (V. B. Kostov et al. 2019), all of which are smaller than $1.6 R_{\oplus}$ with orbital periods shorter than 7.45 days. Additionally, there is a fourth confirmed planet that does not appear to transit, and a candidate fifth planet that is also nontransiting (O. D. S. Demangeon et al. 2021). The three transiting planets (planets b–d) have measured masses of $0.40 \pm 0.14 M_{\oplus}$, $2.2 \pm 0.3 M_{\oplus}$, and $1.9 \pm 0.3 M_{\oplus}$, and radii of $0.85 \pm 0.06 R_{\oplus}$, $1.4 \pm 0.1 R_{\oplus}$, and $1.5 \pm 0.1 R_{\oplus}$ (R. Cloutier et al. 2019; V. B. Kostov et al. 2019; O. D. S. Demangeon et al. 2021), confirming the bulk terrestrial composition of L 98-59 b and L 98-59 c and alluding to a significant gaseous envelope for L 98-59 d. The two outer transiting planets (planets c and d) are prime targets for atmosphere characterization because they have some of the highest transmission spectroscopy metric and emission spectroscopy metric (E. M. R. Kempton et al. 2018; D. Pidhorodetska et al. 2021a) values of any small planet. L 98-59 provides an excellent opportunity to probe the atmospheres of planets smaller than $1.5 R_{\oplus}$ that formed and evolved in the same stellar environment.

We were awarded 28 orbits on the Wide Field Camera 3 (WFC3) instrument on HST to observe five transits of L 98-59 b, and one transit each of planet c and d. No evidence of atmospheric features was seen in the spectrum of L 98-59 b (M. Damiano et al. 2022). In this paper, we report on the HST observations of L 98-59 c. We modeled the spectrum using two different approaches with a goal of identifying whether or not we could definitively detect and place constraints on an atmospheric signal. We also explored the stellar activity of the star, and compared the observations of L 98-59 c with observations of L 98-59-b that were obtained 12.5 hr apart to look for the presence of stellar contamination that might impact both observations. The properties of L 98-59 and the two inner planets (b and c) are summarized in Table 1.

2. Data Analysis

A transmission spectrum of L 98-59 c was measured from a single transit observed with HST/WFC3 with the G141 grism on 2020 April 7 (HST Program GO-15856, PI: T. Barclay), a visit lasting for four HST orbits. The observations with the grism were in round-trip spatial scanning mode with the GRISM512 subarray, with NSAMP = 4 and the SPARS25 sampling sequence. Each spatial scan lasted 69.62 s, and the visit was preceded by a 1.71 s image collected in the F130N filter. All HST data used in this paper are archived at the Barbara A. Mikulski Archive for Space Telescopes (MAST): 10.17909/fe8t-na27.

We used a version of the custom HST WFC3 data and light-curve analysis pipeline described in K. B. Sheppard et al. (2021), nicknamed DEFLATE (Data Extraction and Flexible Light curve Analysis for Transits and Eclipses).²⁰ DEFLATE uses the *ima.fits* files from the MAST but separates the forward and reverse scans for independent processing, since the spatial scans tend to be offset in the spatial direction by several rows, complicating aperture determination. DEFLATE then eliminates the background noise in each exposure using the "difference reads" method (D. Deming et al. 2013). While it is possible to use a scaled version of a master sky background file to remove specific background patterns (M. Gennaro et al. 2018), the method we used takes advantage of the multiple

²⁰ The DEFLATE source code is available on Github at <https://github.com/AstroSheppard/WFC3-analysis>.

Table 1
L 98-59 System Stellar and Planetary Properties, Adopted from O. D. S. Demangeon et al. (2021)

	Parameter	L 98-59
Stellar	Radius (R_{\odot})	0.303 ± 0.026
	Mass (M_{\odot})	0.273 ± 0.030
	T_{eff} (K)	3415 ± 135
	$\log g_s$ (cgs units)	4.86 ± 0.13
	[Fe/H]	-0.46 ± 0.26
	Distance (pc)	10.6194 ± 0.0032
		L 98-59 b
Orbital	R_p/R_s	0.02512 ± 0.00072
	a/R_s	15.0 ± 1.4
	i (deg)	87.7 ± 1.2
	T_c (BJD-2457000)	1366.17067 ± 0.00036
	ρ (g cm $^{-3}$)	3.6 ± 1.5
	P (days)	2.2531136 ± 0.0000015
Planet	$R_p (R_{\oplus})$	0.850 ± 0.061
	$M_p (M_{\oplus})$	0.40 ± 0.16
	$T_{\text{eq},A} = 0$ (K)	627 ± 36
	a (au)	0.02191 ± 0.00084
		L 98-59 c

readouts within each exposure to remove background in a purely data-defined way. As a final step, the pipeline propagates the uncertainty due to this background subtraction by adding it in quadrature, since the new count for each pixel is $F_{\text{new}} = F_{\text{old}} - F_{\text{bkg}}$. The difference reads method lowers the likelihood of cosmic rays impacting the data (since the location of the source on the detector has no bearing on cosmic rays, any ray that hits a nonsource pixel during the observation is automatically zeroed out). It also allows for resolving the source from companions or other field sources in the case of overlapping scans since the individual difference frames do not overlap.

Due to distortions, the pixel-to-wavelength calibration (i.e., wavelength solution) depends on the exact X and Y position on the detector, and so it varies between observations. Still, it is a roughly linear conversion that follows the following set of equations (H. R. Wakeford et al. 2013):

$$\lambda_{(X_{\text{ref}}, Y_{\text{ref}})} = \lambda_{\text{ref}} = a_0 + a_1 * X_{\text{ref}}, \quad (1)$$

$$\lambda_{\text{pixel}} = \lambda_{\text{ref}} + Y_{\text{dispersion}} * (X_{\text{pixel}} - X_{\text{shift}}). \quad (2)$$

The reference coordinates (X_{ref} , Y_{ref}) were determined by the photometric images taken at the beginning of each visit. Coefficients for converting this reference pixel to a reference wavelength (a_0 , a_1) were determined empirically by H. Kuntschner et al. (2009, Table 5). The wavelength of light recorded by a particular pixel is dictated by the dispersion for the Y -coordinate of the reference pixel ($Y_{\text{dispersion}}$) and the intrinsic offset (X_{shift} , in pixels) between the location of the filter image and the grism-dispersed light. $Y_{\text{dispersion}}$ and X_{shift} are constrained, but the spatial scan mode complicates those values. Consequently, DEFLATE fits for these values by comparing an observed out-of-transit spectrum to an ATLAS stellar model (F. Castelli & R. L. Kurucz 2004) multiplied by the G141 grism sensitivity curve. The stellar model combines the line and continuum fluxes as ($\alpha \times \text{line} + \text{continuum}$), essentially allowing the strength of the stellar lines to vary to compensate for metallicity or other opacity mismatches. Figure 1 shows the result of the fit for L 98-59 c.

We determined the wavelength solution separately for both the forward-scan and reverse-scan light curves. The forward

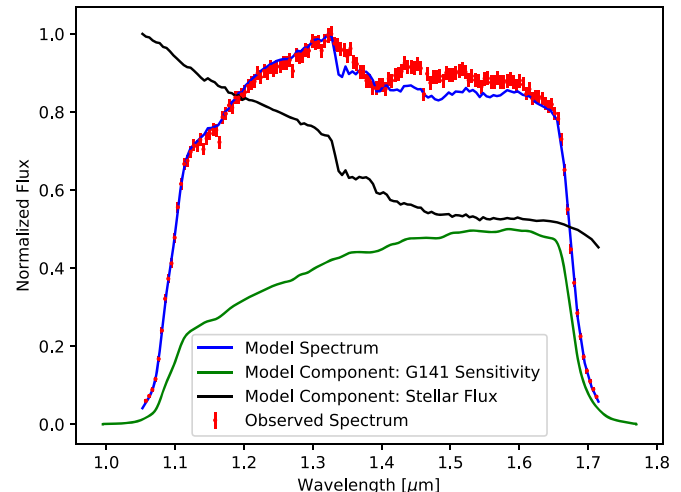


Figure 1. The model we generated for the stellar spectrum provides a sufficient match to the observed spectrum over the G141 wavelength range for use in our wavelength calibration.

and reverse scans tend to be offset vertically from one another by a small amount, and the difference in wavelength solution is never more than 3% and typically around 1.5%, well within the size of a detector pixel (i.e., subpixel shift). We found that the wavelength solution was not significantly impacted by exact stellar model choice, error scaling, or line-strength scaling.

DEFLATE uses the downloadable WFC3 flat-field files to divide out the flat-field from both the data and the error array (to propagate uncertainty), and removes the cal-wfc3-flagged “bad” pixels (which are identical across all exposures) by giving them zero weight. It is possible to interpolate flux values at these pixels, but we preferred the zero-weight method since it requires fewer assumptions. The zero-weight pixels make up roughly 2% of all pixels in an exposure. DEFLATE also uses a corrected median time filter to flag cosmic rays. Before applying the filter, DEFLATE normalizes each pixel by the median of its row, which prevents DEFLATE from flagging entire rows as cosmic rays since they are distorted by time-dependent instrumental effects, inconsistent spatial scan rates, and obviously the transit/eclipse itself. We then used a double-

sigma cut, first applying an 8σ cut to remove any extreme outliers, then applying a second 5σ cut to correct the remaining energetic particles. Less than 0.5% of all pixels in L 98-59 c's observations were impacted by cosmic rays, and typically only a few pixels per exposure were impacted.

Finally, DEFLATE follows a simple procedure to define a light-curve extraction aperture. It first defines the maximum flux of an exposure as the median of the five rows with the greatest flux. The edge of the box is set to the outermost row and column with a median value of greater than 3% of the maximum flux. This relatively low cutoff captures the entire first-order spectrum and minimizes the impact of vertical shifts. This method maximizes the signal-to-noise ratio (SNR) from the source and avoids overprocessing the data.

3. Light-curve Analysis

Modeling a transit light curve has two major components: modeling the physical transit, and modeling the nonastrophysical instrumental effects related to how the WFC3 instrument collects flux, i.e., the instrumental systematics. WFC3 observations commonly exhibit several instrumental effects; the most prominent effects are a hook/ramp feature due to charge-trapping, a visit-long decrease in flux, a “breathing” effect based on changing temperatures during HST’s orbit, and a wavelength jitter effect (e.g., Z. K. Berta et al. 2012; H. R. Wakeford et al. 2016; Y. Zhou et al. 2017; A. Tsiaras et al. 2018, among many others). These features vary in magnitude across different observations in nonobvious ways. There is no encapsulating physically motivated model to describe all of these effects (though recently individual features have been modeled more successfully; e.g., Y. Zhou et al. 2017). Instead of using the inherent properties of the detector, these features are typically removed using empirical methods (N. P. Gibson 2014; N. Nikolov et al. 2014; K. Haynes et al. 2015). For this work, we used a new version of parametric marginalization, a Bayesian model averaging strategy that was conceptually introduced to exoplanet light curves by N. P. Gibson (2014) and first applied to WFC3 transit spectroscopy by H. R. Wakeford et al. (2016).

Similar to H. R. Wakeford et al. (2016), we found that fourth-order polynomial parameterization consistently described the systematic effects while preserving computational time. We used a grid of models that included up to four powers of phase (ϕ_{HST}) and four orders of wavelength shift. Of the five forms of orbital-phase-dependent visit-long slopes (none, linear, quadratic, exponential, and log), we only allowed linear, as discussed in the next section. Each higher power included all lower powers (e.g., the third-order ϕ_{HST} phase is $a_0 \times \phi_{\text{HST}} + a_1 \times \phi_{\text{HST}}^2 + a_2 \times \phi_{\text{HST}}^3$), and there were no cross terms. This resulted in a grid of 25 systematic models (five possible ϕ_{HST} powers \times five possible shift powers \times one possible slope parameterization). There were two additional parameters, separate normalization constants for the forward (A_f) and reverse scans (A_r).

To efficiently obtain light-curve parameter values and uncertainties, we followed the methodology presented in K. B. Sheppard et al. (2021) and fit each model using KMPFIT.²¹ Each model was then weighted by its Bayesian evidence and marginalized over the model grid.

We used the BATMAN software (L. Kreidberg 2015) to generate the transit models that were used for the astrophysical

component of the light-curve model. The model strongly constrained the transit depth (R_p/R_s) and center-of-transit time (T_0), with weak constraints on scaled semimajor axis (a/R_s), inclination (i), and a linear limb-darkening coefficient (c_0). We assumed a four-parameter nonlinear limb-darkening (LD) and derived the coefficients by interpolating values from A. Claret et al. (2012) to the central wavelength of WFC3 (1.4 μm). These coefficients were fixed for light-curve fitting as HST’s poor phase coverage does not well constrain the shape of transit. We also compared the LD values with earlier models by A. Claret & S. Bloemen (2011) to be sure the results are not sensitive to LD source and also tested a linear LD law with the coefficient being a fitted parameter.

We first fit a model to the white-light light curves, which provided a confidence check on the data, maximized SNR for deriving wavelength-independent properties such as inclination and a/R_s , and captured the structure of residuals for each systematic model, if present. Determining the residuals allowed further detrending of spectral curves via white-light residual removal (D. Deming et al. 2013; A. M. Mandell et al. 2013; K. Haynes et al. 2015). While this method is suitable for M-dwarf targets that are near constant flux across the bandpass (including L 98-59, despite the small variations in flux we see in Figure 1), this method is not generally applicable to hotter stars. We fixed the orbital period, inclination, and a/R_s to their values in Table 1, and only allowed linear visit-long slopes, since the L 98-59 data set only had three usable orbits covering a small amount of the out-of-transit baseline.

The unprocessed light curve, along with the light curve with instrumental systematics removed, and the residuals when the highest-weighted systematic model was subtracted from the instrumentals-subtracted light curve are shown in Figure 2. The derived transit depths and center-of-transit times (T_c) are given in Table 2. The white-light depth was measured to be 1620 ± 24 ppm. The derived depths are insensitive to model assumptions, varying less than 10 ppm when either a linear LD or a/R_s was included in the model as fitted parameters (significantly less than 1σ), or if a quadratic visit-long slope was assumed. The reduced chi-squared (χ^2) of each fit was around 1.2, which is typical of HST white-light light curves.

To further validate these results, and to make sure the derived uncertainties are reasonable, we fit the highest-weighted systematic model of L 98-59 c using a Markov Chain Monte Carlo approach (emcee; D. Foreman-Mackey et al. 2013). The model successfully converged, and we found that the posteriors, such as the transit depth, exhibit Gaussian distributions. We derived uncertainties slightly smaller than those obtained with KMPFIT, which are shown in Table 2. The two methods are in excellent agreement, down to the parts-per-million (ppm) level: both estimate a depth of 1620 ppm, with the MCMC uncertainty being 98% of the KMPFIT uncertainty. However, when the impact of using multiple models in the KMPFIT method is included, the uncertainty inflates from 11 to 24 ppm. We have adopted this larger uncertainty. Notably, the overall white-light uncertainty in Table 2 is larger due to the effects of model marginalization. Correlations were not seen with any nonastrophysical light-curve parameters.

We binned the 1D spectra from each exposure in the region covered by the grism response curve (1.1–1.6 μm) to compute spectral-photometric time series for each spectral bin (shown in Figure 3). We tested several bin widths since the long scan observations (close to 300 rows) are more at risk of wavelength

²¹ KMPFIT is available as part of the Kapteyn Package, available at <https://github.com/kapteyn-astro/kapteyn/>.

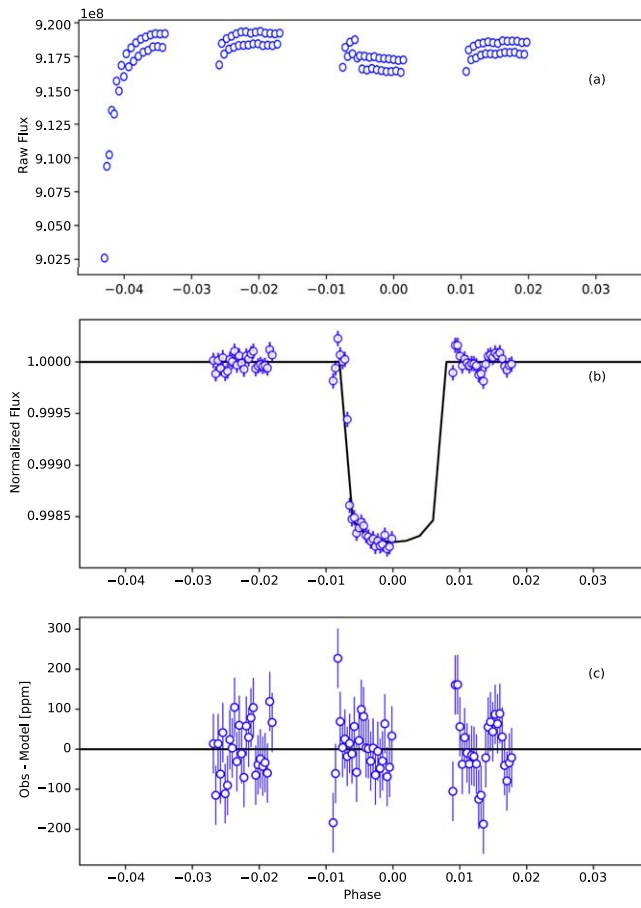


Figure 2. Visualization of white-light light-curve fit for the highest-weighted systematic model for L 98-59 c, which demonstrates a good model fit to the observed data. Panel (a) shows the band-integrated light curve. Panel (b) shows the detrended light curve as well as the best-fitting transit model. The instrumental effects and transit model parameters were fit for simultaneously. Panel (c) shows the residuals between the data and the best-fitting model.

Table 2
L 98-59 c White-light Light-curve Measured Transit Parameters

Observation	Transit Depth (ppm, $(R_p/R_s)^2$)	T_c (BJD-2457000)
L 98-59 c	1620 ± 24	1946.7068 ± 0.0001

blending (A. Tsiaras et al. 2016), which will affect larger bins less than smaller ones. We find no difference as a function of bin width (see Figure 4), and we choose 6 pixel wide ($0.0279 \mu\text{m}$) bins to maximize resolution without drowning the signal in noise. The spectrum is given in Table 3, and the spectral time series data are shown in Figure 3.

Following K. B. Sheppard et al. (2021) we looked into three different methods to assess the robustness of our analysis: (1) the goodness-of-fit of the highest-weighted systematic model for each light curve using the reduced χ^2 statistics, (2) a residual normality test, and (3) whether red noise was present in the light-curve residuals, as that could bias inferred transit depths (P. Cubillos et al. 2017).

For both the band-integrated (white light) and spectrally binned light curves we measured reasonable reduced χ^2 values that ranged between 0.7 and 1.4. The band-integrated analysis ($\chi^2_\nu = 1.2$) and all spectral bins (median $\chi^2_\nu = 0.9$) fall within

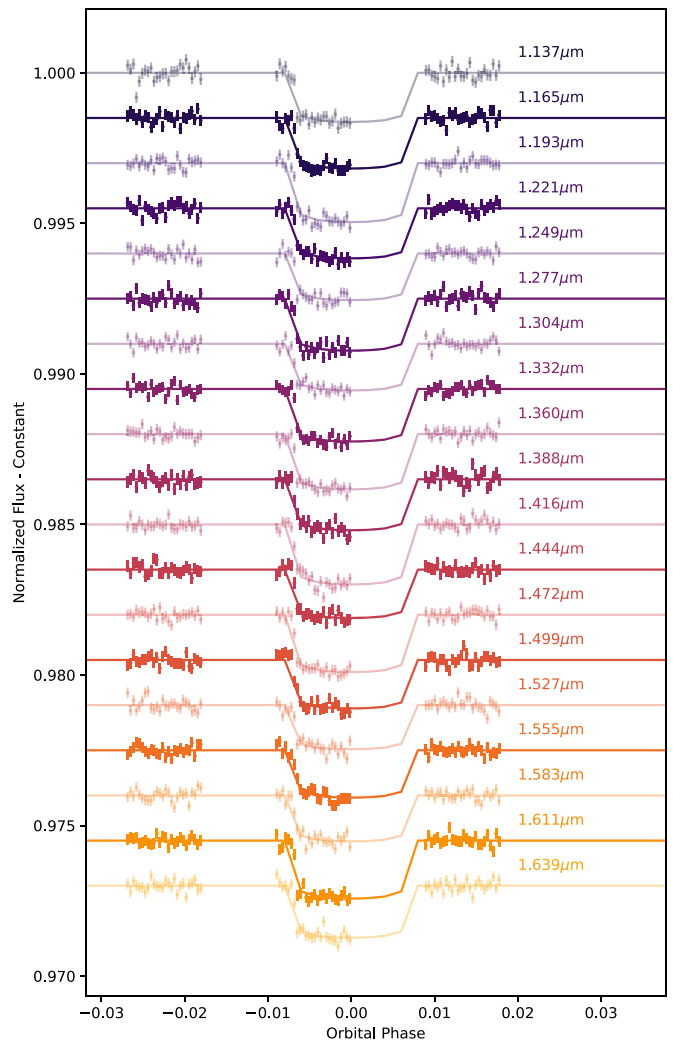


Figure 3. Spectral time series data for L 98-59 c, collected during the first visit; systematic variations have been removed.

the expected range, except for the 1.499 μm light curve. The reduced χ^2 of this bin is 0.59, which likely indicates that the uncertainties in this light curve are overestimated, probably due to incorporating white-light residuals that inflated uncertainties.

A residual normality test assesses whether the residuals for a model are Gaussian distributed. We used the `scipy` implementation of the Shapiro–Wilk test for normality (S. S. Shapiro & M. B. Wilk 1965; P. Virtanen et al. 2020). Normality is rejected at the 5% significance level only for the 1.14 μm spectral bin residuals, and in this case this is owing to a single outlier. Removing this outlier enabled us to recover a consistent depth and uncertainty, and the residuals are consistent with normality. Further, ignoring residuals recovered almost the exact same transit depth without any normality issues. We retained this exposure in our analysis.

Finally, we tested for correlated noise in the residuals following the time-averaging methodology of P. Cubillos et al. (2017; see also F. Pont et al. 2006) and using MC³²². Noise can be thought of as the sum of a purely random (white) noise and a time-correlated (red) noise: $\sigma_{\text{total}} = \sqrt{(\sigma_w^2/N + \sigma_r^2)}$ (F. Pont et al. 2006). As normally distributed residuals with a mean of zero (i.e., if uncorrelated white noise is the dominant

²² The MC³ software is available from <https://github.com/pcubillos/mc3>.

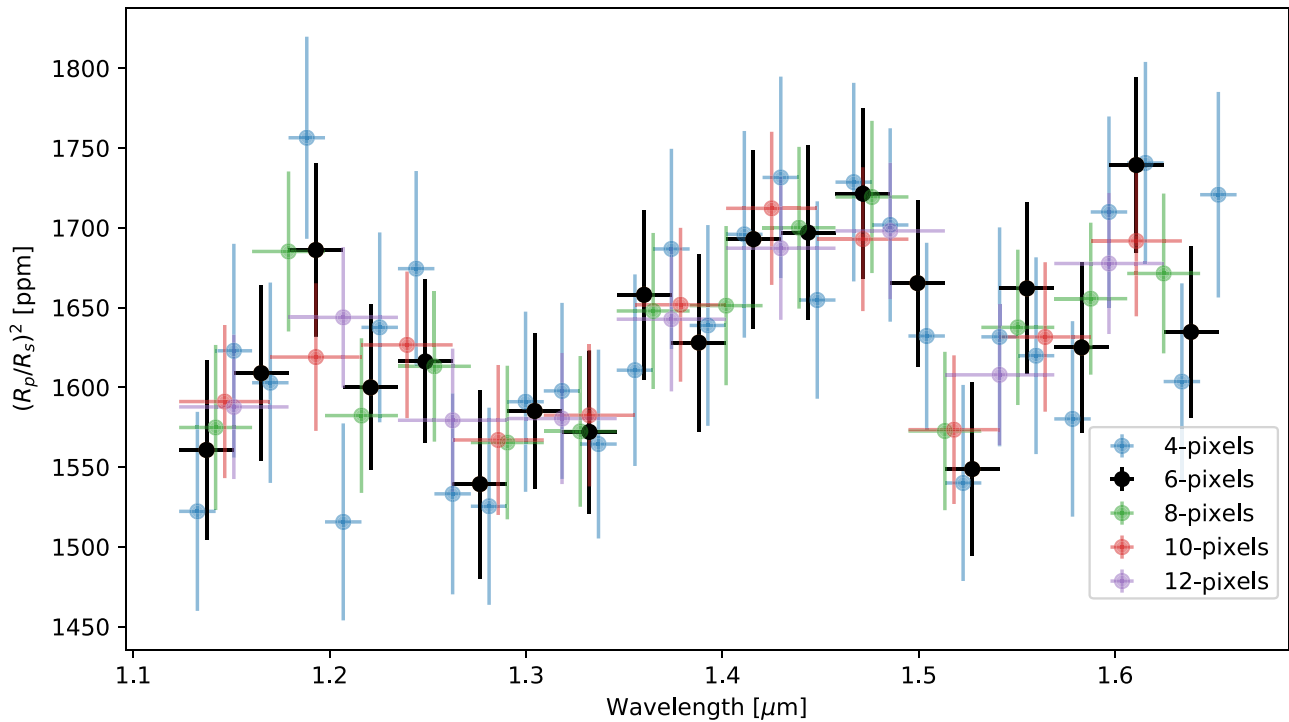


Figure 4. The marginalization-derived transit spectrum for L 98-59 c at different resolutions, in which all show evidence for a nonflat spectrum. The shape of the spectrum is not sensitive to the spectral bin size.

Table 3

Transmission Spectra of L 98-59 c, with Bin Size $0.0279 \mu\text{m}$ and Resolution ~ 50

λ (μm)	Depth (ppm)
1.123–1.151	1561 ± 56
1.151–1.179	1609 ± 55
1.179–1.207	1686 ± 54
1.207–1.235	1600 ± 52
1.235–1.263	1616 ± 51
1.263–1.291	1539 ± 59
1.291–1.318	1585 ± 49
1.318–1.346	1572 ± 51
1.346–1.374	1658 ± 53
1.374–1.402	1628 ± 56
1.402–1.430	1693 ± 56
1.430–1.458	1697 ± 55
1.458–1.485	1721 ± 53
1.485–1.513	1665 ± 52
1.513–1.541	1549 ± 54
1.541–1.569	1662 ± 54
1.569–1.597	1625 ± 54
1.597–1.625	1739 ± 55
1.625–1.653	1635 ± 54

uncertainty source) are averaged in time, the scatter in the points decreases proportional to σ_w/\sqrt{N} . If red noise is significant, then the time-averaging only decreases noise until it flattens out at σ_r . One can test for the impact of red noise by time-averaging the residuals and comparing the resulting rms function to theoretical expectations of white noise. We enhanced this method by simulating synthetic normally distributed residuals with the same standard deviation as the actual residuals, and putting them through the same method

(Figures 5 and 6). We note the 1 and 2σ bands for random, pure white-noise residuals compared to the results for the actual residuals. For every bin the residuals are consistent with random white noise for every bin size. We find no evidence of correlated noise.

Figure 6 shows a visualization of the correlated noise test by looking at the autocorrelation function of the residuals. This method is not purely quantitative, but can provide another look at potential structure in the residuals. The red lines in Figure 6 indicate the 2σ line—roughly indicating “significant” correlations at that lag. A few lags crossing this threshold is not concerning, since 2σ events happen roughly 5% of the time and we are sampling many bins. This is less quantitative, but autocorrelation functions that appear too structured can be, unsurprisingly, indicative of structured noise. An example is the $1.165 \mu\text{m}$ bin, which resembles a decreasing sinusoid. However, structure below significance is less problematic. Different systematic model selections from the highest-ranking models give the same transit depth at this bin without structured residuals, and it passes the other red-noise test, so we have confidence in the depth determination.

4. Exploratory Analysis of Potential Atmospheres with PLATON

In the subsequent sections, we study whether the apparent structures in the spectra of L 98-59 c are significant and indicative of an atmosphere with a reasonable chemical composition. Only a low-mean-molecular-weight atmosphere could produce spectral features with amplitudes similar to the features seen in our results (roughly 100 ppm). However, due to the relatively large error bars on each individual spectral bin, it is not obvious that a model with molecular features would be a significantly improved fit over a straight line (indicative of no

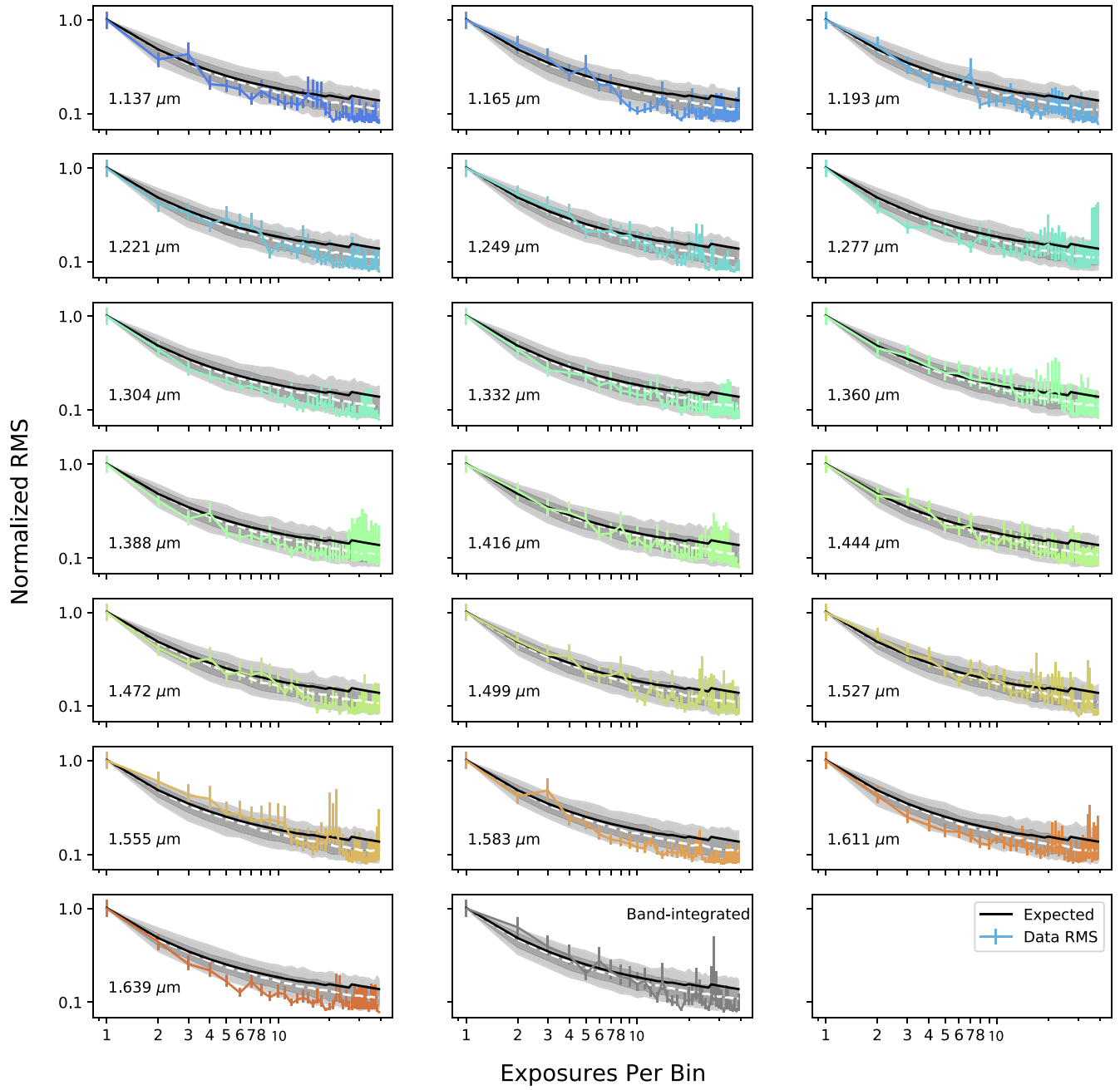


Figure 5. Binned rms analysis for each spectral bin, which shows no evidence of red noise. The rms of the data residuals are shown by the colored lines. The solid black line is the theoretical trend from P. Cubillos et al. (2017). The dashed white line is the median value from simulated pure white-noise residuals. The gray regions are the 1 and 2σ ranges for the simulated white-noise residuals, which demonstrates that the observed data are consistent with being largely uncorrelated (e.g., white noise).

atmosphere, an atmosphere with a high mean molecular weight, or high-altitude clouds).

We utilized two different strategies to investigate the potential for detecting an atmosphere. We first used the open-source retrieval tool PLATON (M. Zhang et al. 2019) to perform a Bayesian statistical retrieval of the atmospheric parameters assuming an H₂-rich composition (about 1%–2% by mass; E. D. Lopez & J. J. Fortney 2014) and equilibrium chemistry. We then examined the ability to constrain the presence of individual molecular constituents using a more simplistic fitting scheme for combinations of individual absorbers with the Planetary Spectrum Generator (PSG; G. L. Villanueva et al. 2018).

4.1. PLATON Atmospheric Modeling and Retrieval Methodology

PLATON is open-source retrieval software developed by M. Zhang et al. (2019), which comprises a forward model and an algorithm for Bayesian inference. Though there are minor differences, it essentially uses the same forward model as ExoTransmit (E. M. R. Kempton et al. 2017). The software assumes an H₂-He-dominated atmosphere, and though it has recently incorporated free-retrieval capabilities, in this study we exclusively used the version which assumes chemical equilibrium. Though these constraints naturally limit the types of planetary atmospheres that can be explored, it was useful in

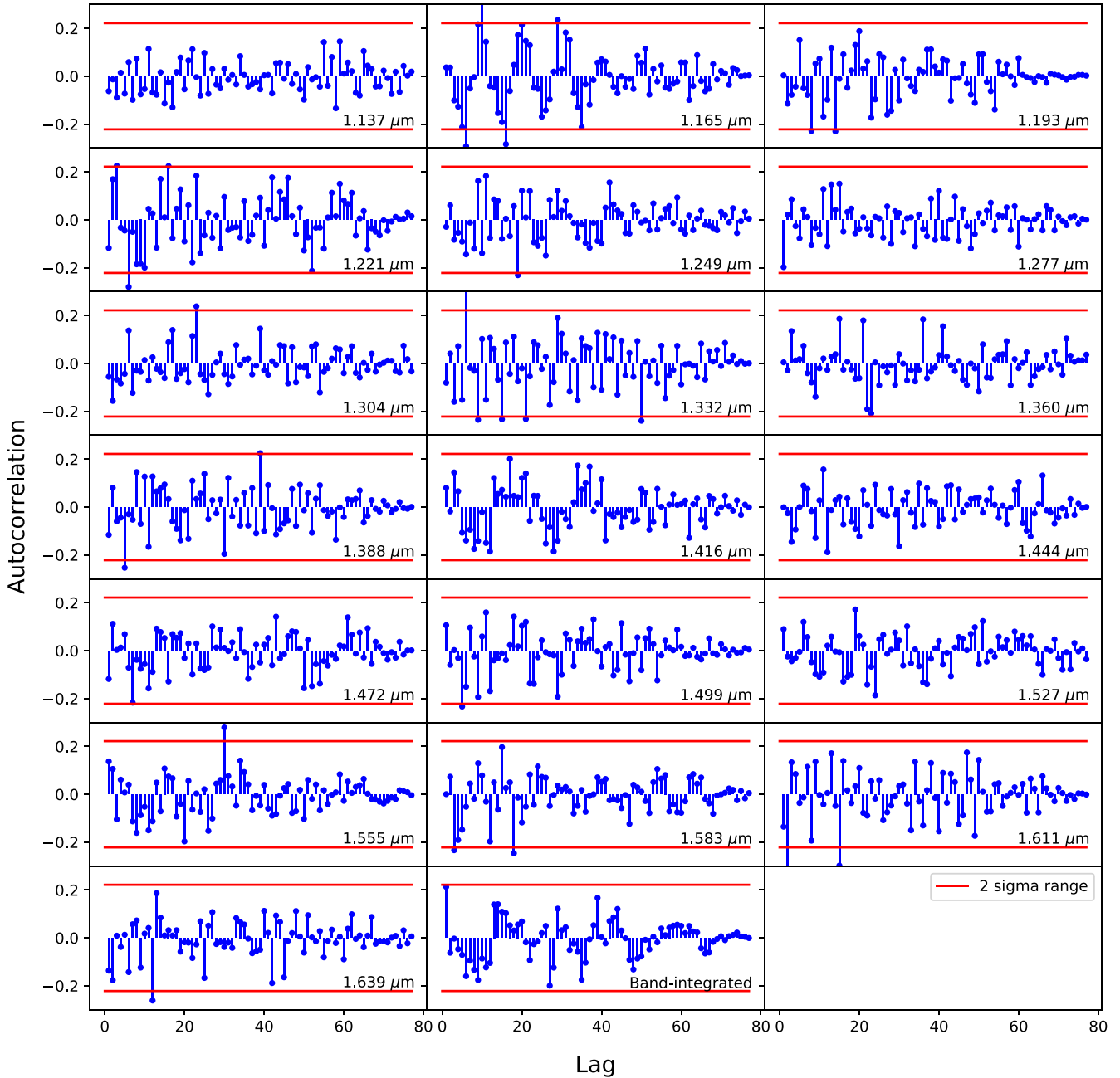


Figure 6. The autocorrelation function of the residuals for each spectral bin. The blue lines and dots show the autocorrelation function as a function of lag, with lag 0 left out for clarity. The solid red lines indicate the 2σ range; autocorrelation values within these lines are not considered significant. The observed data have minimal significant autocorrelation.

contextualizing the spectrum and investigating the likelihood of an H₂-dominated atmosphere on L 98-59 c.

Table 4 describes the parameters and their priors for the PLATON atmospheric retrieval. We allowed planet radius, C/O, metallicity, temperature, and cloud-top pressure to vary, and assumed an isothermal temperature profile. C/O and metallicity dictate the elemental ratios in the atmosphere, which are input with temperature into a chemical equilibrium code (GGchem; P. Woitke et al. 2018) to determine the abundance of every species at every pressure layer. Each chemical parameter was given a prior set by computational limits (most notably $T_{\min} = 300$ K), and the mass/radius priors were set by literature values (O. D. S. Demangeon et al. 2021); we included stellar radius and planetary mass in order to propagate the

literature uncertainties forward. The retrieval utilized nested sampling (J. Skilling 2004; J. S. Speagle 2020) with 200 live points to sample the parameter space and calculate a Bayesian evidence for the model.

4.2. PLATON Retrieval Results

The retrieval finds a best model fit with $\chi^2_{\text{Red}} = 1.15$, with 8 degrees of freedom. The resulting posterior distributions and best-fit model spectra from the retrieval are shown in Figure 7. Under the assumption that L 98-59 c has an H₂-dominated atmosphere with no disequilibrium processes, L 98-59 c was best described as a high-metallicity atmosphere ($Z \sim 250 \times Z_{\odot}$) with a likely supersolar C/O ratio. The

Table 4
Priors for Parameters Used in L 98-59 c Equilibrium Retrievals

Parameter	Symbol	Prior Dist.
Planet radius (R_{\oplus})	R_p	$\mathcal{U}(0.7, 2.1)$
Limb temperature (K)	T	$\mathcal{U}(300, 1100)$
Carbon-to-oxygen ratio	C/O	$\mathcal{U}(0.05, 2.0)$
Metallicity	Z	(−1, 3)
Planet mass (M_{\oplus})	M_p	$\mathcal{N}(2.22, 0.26)$
Stellar radius (R_{\odot})	R_s	$\mathcal{N}(0.30, 0.02)$
Cloud-top pressure (Pa)	P_{cloud}	$\mathcal{LU}(-3, 8)$
Stellar effective temperature (K)	T_{\star}	Fixed (3429 K)
Spot temperature (K)	T_{spot}	Fixed (2920 K)
Spot covering fraction	f_{spot}	$\mathcal{U}(0, 0.5)$

Note. \mathcal{U} refers to a uniform prior, \mathcal{LU} a log uniform prior, and \mathcal{N} a normal prior.

retrieved atmospheric metallicity was consistent with predictions from the hypothesized mass–metallicity relationship from the solar system planets (e.g, J. J. Fortney et al. 2013), and the retrieved R_p was consistent with the literature ($1.30 \pm 0.07 R_{\oplus}$). The atmospheric temperature was poorly constrained, which is expected for a retrieval of transmission spectrum, and the cloud-top pressure was also weakly constrained due to the narrow wavelength coverage and the large uncertainties on the data. The best-fit model yielded small water features at $1.4 \mu\text{m}$ and $1.1 \mu\text{m}$, but there was no statistically significant water detection. We note that the inferred water feature at $1.4 \mu\text{m}$ is roughly 100 ppm, which is consistent with predictions of the feature size for an H_2 -dominated atmosphere, assuming 4 scale heights (derived from L. Kreidberg 2018), but somewhat larger than what we would expect at 2 scale heights (A. R. Iyer et al. 2016; G. Fu et al. 2017; H. R. Wakeford et al. 2019; P. Gao et al. 2020).

PLATON also allows for model comparison, since nested sampling naturally calculates the Bayesian evidence of a model. Although this evidence cannot act as an absolute goodness-of-fit metric, the ratio of two evidences provides a straightforward measure of how much more likely one model is in comparison to the other. This ratio is known as the odds ratio ($\mathcal{O}_{12} = \mathcal{Z}_1 / \mathcal{Z}_2$), and is directly interpreted as “Model 1 is $\mathcal{O}_{12} \times$ more probable than Model 2.” There are also empirically determined benchmarks for converting \mathcal{O} into more familiar sigma-level significance (R. Trotta 2008; B. Benneke & S. Seager 2013).

To determine the likelihood of an H_2 atmosphere on L 98-59 c, we compared the evidence of the retrieved fiducial atmosphere to that of a flat line spectrum. We introduced a flat spectrum into PLATON by fixing a very high, gray cloud. We then only allowed planet radius to vary in the fit. The resulting fit is shown in the upper-right panel of Figure 7. The odds ratio between the fiducial model and the flat-spectrum model was 3, which corresponds to a “weak” detection of roughly 2.1σ in favor of the fiducial model over the flat-spectrum model, or about 75% probability. We note that the specific sigma significance is relatively imprecise, since even a small numerical error in \mathcal{Z} —which is common (J. S. Speagle 2020)—could shift the odds ratio slightly below the empirical cutoff. We also compare the Bayesian evidences between the fiducial atmosphere and the same atmospheric model with no water opacity, finding the odds ratio to be ~ 1 . This indicates

that there is no conclusive evidence of the presence of water vapor in the atmosphere. The evidence of water vapor specifically is weaker than that of the full atmosphere model since other opacity sources (e.g., NH_3) can “fill in” for water vapor and capture some of the structure in the observed spectrum.

5. Planetary Spectrum Generator Atmospheric Modeling and Retrieval

The PLATON forward model and retrieval framework includes a number of assumptions about the atmospheric composition and structure that limit the ability to examine the evidence for individual atmospheric absorbers. For these reasons, we also opted for an exploratory model-fitting approach using PSG in which we analyze the potential for a molecular detection by looking at how well simulated spectra with a number of potential atmospheric absorbers fit the data. To quantify the goodness of the fit, we used the reduced χ^2 (χ^2_{red}) of the data and the model, and we examined the χ^2_{red} across a range of molecular combinations and abundances.

PSG (G. L. Villanueva et al. 2018, 2022) is a radiative transfer model and tool for synthesizing/retrieving planetary spectra (atmospheres and surfaces) for a broad range of wavelengths (50 nm to 100 mm, UV/vis/near-IR/IR/far-IR/THz/submillimeter/radio) and includes predefined templates for a large variety of instruments and observatories. As part of the retrieval framework of PSG, the tool has access to nested sampling and optimal estimation retrieval algorithms (C. D. Rodgers 2000) to analyze planetary data and retrieve atmospheric/surface/physical parameters of interest via minimization of spectral residuals.

Simulated spectra with PSG include molecular, atomic, aerosol, and continuum (e.g., Rayleigh, Raman, collision-induced absorption) radiative and scattering processes, which are implemented via a layer-by-layer framework. Many spectral databases are available in PSG, but for this study we have employed the molecular parameters from the latest HITRAN-2020 database (I. Gordon et al. 2022) that are implemented using a correlated- k method (21 molecular species are included). A list of the molecular and atomic databases (including HITRAN) are provided online, along with the specific molecules used, assumptions made, capabilities, and references.²³ The HITRAN molecular database is complemented in the UV/optical with cross sections from the Max Planck Institute of Chemistry database (H. Keller-Rudek et al. 2013). Besides the collision-induced absorption (CIA) bands available in the HITRAN database, the MT_CKD water continuum is characterized as $\text{H}_2\text{O}-\text{H}_2\text{O}$ and $\text{H}_2\text{O}-\text{N}_2$ CIAs (V. Kofman & G. L. Villanueva 2021). For this simulation we omitted aerosols (clouds, haze, etc.), and removed all molecules other than the two we wished to explore for any given simulation. The structure of the atmosphere was described in PSG by specifying for each layer the pressure (in bar), temperature (in kelvin), and the abundances of atmospheric constituents with respect to the total gas content. For each gas, layer-by-layer integrated column densities (molecules per square meter) were then computed along the transit slant paths employing a pseudo-spherical and refractive geometry. We assumed the molecule abundance was held to a consistent volume mixing ratio (VMR) throughout the

²³ psg.gsfc.nasa.gov

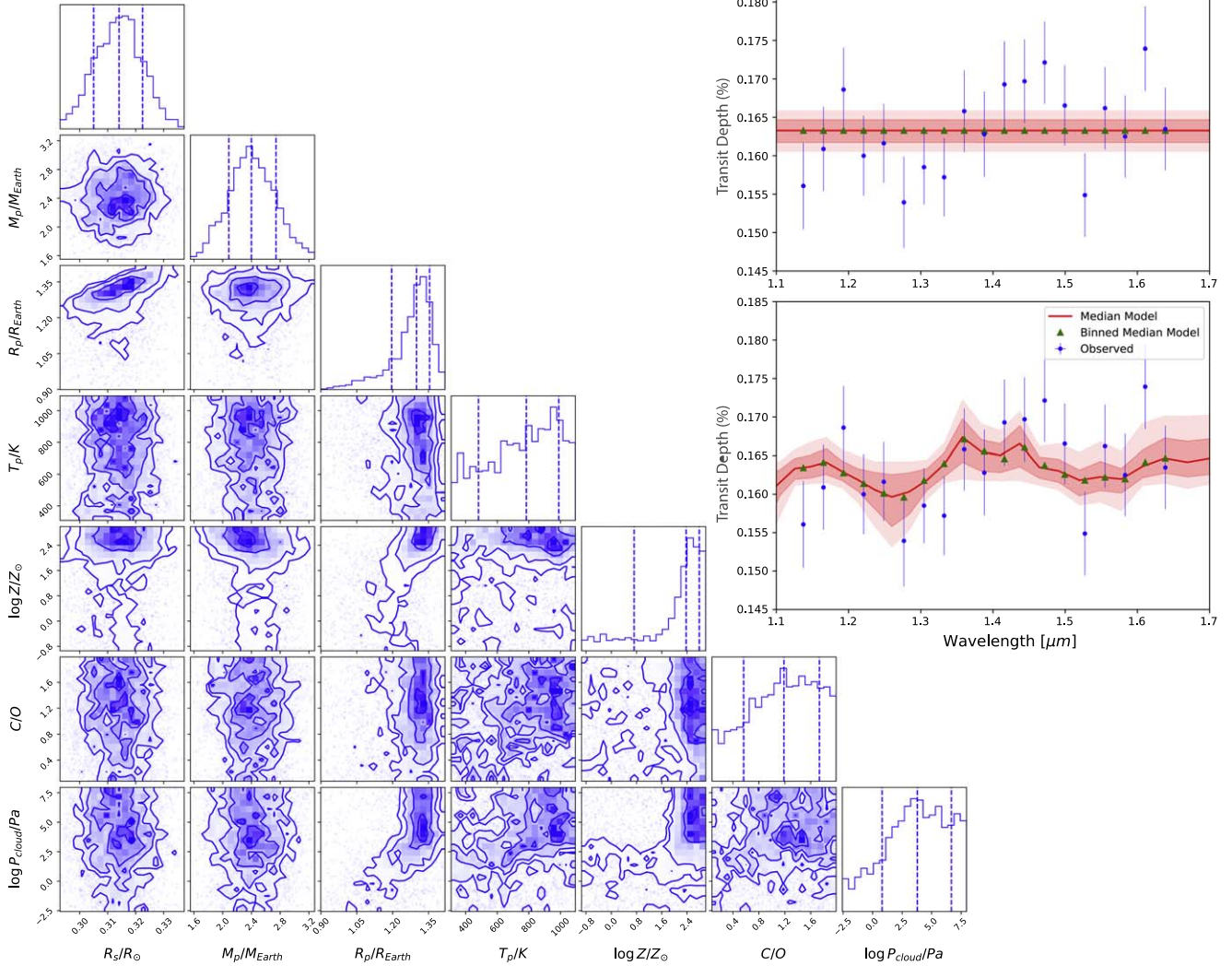


Figure 7. Retrieval results for L 98-59 c. Left: corner plot for the best-fit fiducial H₂-dominated atmosphere. Upper right: best fit assuming a flat spectrum (high clouds or no detectable atmospheric features). Lower right: model spectrum assuming the median retrieved parameter values (green triangles) with 1 and 2 σ contours (red) plotted over data (blue).

atmosphere; however, the temperature–pressure profile was defined using the V. Parmentier & T. Guillot (2014) analytic gray opacity model.

5.1. Chi-squared Analysis Methodology

As previously pointed out, the large error affecting each spectral bin may be too large to clearly discern the abundance of gaseous species of interest by working with a classical retrieval approach, in which one tries to constrain abundance and uncertainty simultaneously for a set of species. In addition, the spectral resolution is low enough that it would be challenging to uniquely distinguish molecular signatures from the spectral continuum.

For these reasons we have opted for an “upper-limit” approach, in which we calculate the statistical significance of models including different individual molecular species, and determine the abundance at which point the molecule would be detected. The natural metric to quantify the goodness of the fit is the χ^2_{red} of the model fit (where χ^2_{red} consists of the χ^2 divided by the degrees of freedom). A χ^2_{red} of 1 is considered to be an optimal fit, which indicates that the model matches the

data to the noise level and the information is being retrieved in its entirety (assuming correct noise estimation). A χ^2_{red} of less than 1 suggests that the uncertainties are overestimated, while a $\chi^2_{\text{red}} > 1$ indicates that either the model is incomplete or the uncertainties are underestimated. The higher above 1 that χ^2_{red} climbs, the less accurate the fit of the data.

To calculate χ^2_{red} , we utilized the optimal estimation retrieval tool in PSG. Errors in computation of normalized residuals can also lead to additional sources of uncertainty, thus PSG calculates the standard deviation of points per residual spectrum in order to better mitigate the effect of error in χ^2_{red} . Each spectral model is produced by fixing the abundance of two gases of interest to specific values, chosen in a given range; we then retrieve the planetary diameter as the only free parameter, as that can be reliably constrained by the average intensity of the observed spectral continuum (as seen in Figure 8); this also lowers our number of additional degrees of freedom to 1. We then produced two-dimensional views of the χ^2_{red} for each combination of gases and their respective abundances; this procedure is repeated for several combinations of gases, yielding a comprehensive view of the likelihood

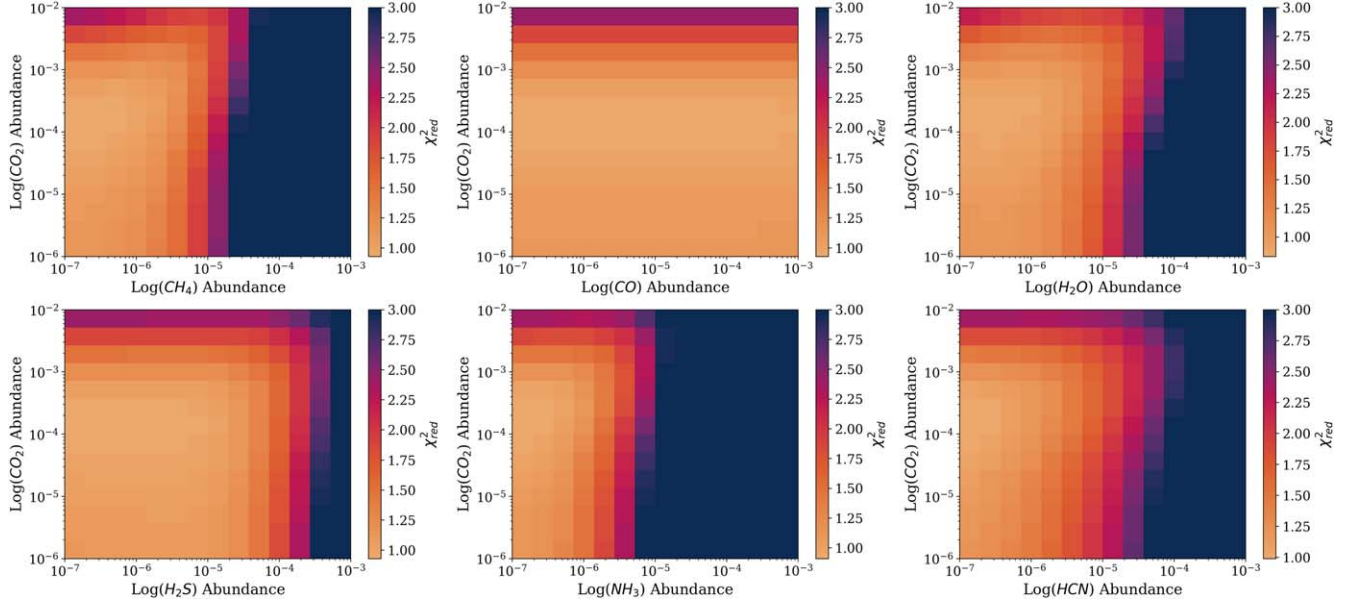


Figure 8. The heat maps above portray the results of a two-molecule atmosphere analysis in terms of VMR. All of the presented analyses have the molecular abundance of CO_2 on the y-axis. In the top left we have CH_4 , in the top middle we have CO , in the top right we have H_2O , in the lower left we have H_2S , in the lower center is NH_3 , and in the lower right we have HCN . We retrieved for diameter at each abundance level, and calculated the χ^2_{red} to find the best-fit retrieval for diameter. The best-fitting models are found at 10^{-4} VMR, or 10^2 ppm, CO_2 abundance and extremely low abundances, 10^{-6} or lower, for other molecules.

that the presence of those specific gases in the atmosphere may well fit the observed spectrum.

Through this process we explored the statistical parameter space to locate regions where the χ^2_{red} value has a minimum. Those gases characterized by a clear minimum in χ^2_{red} in correspondence to a specific concentration are those that are more likely to be present in the atmosphere. Those that do not yield a clear χ^2_{red} minimum for any concentration are likely not detectable above the noise level.

5.2. Results of the PSG Analysis

We explored models with molecular species that are both common to planetary atmospheres and have absorption features in the WFC3 spectral band, with abundances ranging from 10^{-7} to 10^{-2} VMR. CO_2 was assumed to be present in each simulation as a CO_2 -only atmosphere maintained a good fit, while the second molecule varied between five others: CH_4 , H_2O , H_2S , NH_3 , and HCN . We chose to include any molecular species that were present at abundances greater than 1 part per billion (ppb) and had absorption lines within 200 to 1000 nm as trace secondary molecules. We also assumed an H_2 -rich atmosphere, as the combination of an H_2 -rich atmosphere, trace molecules, and no clouds is the most consistent with the observations; the correlated- k opacity tables used in the forward modeling also assume an H_2 -rich atmosphere.

We present in Figure 8 the full range of χ^2_{red} values per molecular pair over the full range of possible abundances per molecule. As can be seen in Figure 8, the lowest χ^2_{red} values (between 0.5 and 1.0) can be found at approximately 10^{-4} VMR, or 10^2 ppm, CO_2 abundance. For each of the other trace molecules this minima is achieved at extremely low abundances of 10^{-6} or lower. While we searched for CO , its high-energy, low-intensity bands in this wavelength range led to no fit improvement or detriment, thus it was not included in further analysis.

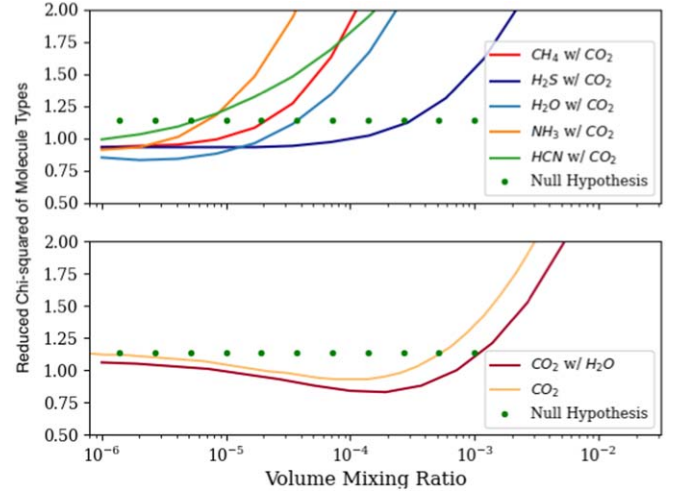


Figure 9. The reduced χ^2 when various different molecules are locked to their best-fit values are shown here. In the top panel, all CO_2 values are locked at approximately 10^{-4} VMR while the other molecules are free. In the lower panel, H_2O is locked at approximately 10^{-6} VMR. The value obtained with a flat transmission spectrum is presented in both panels as a dotted line, portraying the scenario in which there is no atmosphere present. This plot presents at which point every combination of molecules becomes a worse assumption than having no atmosphere, i.e., becomes an unrealistic scenario. The models in the lower panel including CO_2 provide a significantly better description of the data over a wide range of VMRs.

To expand on the results found in Figure 8, Figure 9 examines the direct molecular χ^2_{red} when different molecules are locked to a value. In the top panel of the figure, all CO_2 concentrations are locked at 10^{-4} VMR (i.e., the best-fit value for CO_2 according to our prior χ^2_{red} analysis), and the other molecules are varied across the entire VMR range of 10^{-7} – 10^{-2} . We also plotted the fit wherein we assume there is no atmosphere present, which presents a χ^2_{red} of 1.14, i.e., the null hypothesis. As can be seen, the HCN and NH_3 models

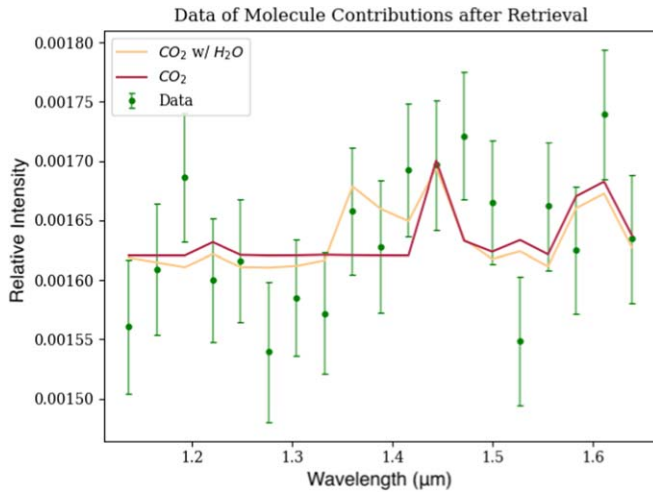


Figure 10. The best retrieval results from Figure 9’s lower panel are presented here along with the observed data and uncertainty to portray the extent to which the model is consistent with the data.

overtake the null hypothesis just before 10^{-5} VMR, and thereafter decrease the goodness of the fit in χ^2_{red} . The CH₄ model overtakes the null hypothesis just after 10^{-5} VMR. These molecules, if present, have extremely low abundances. This leaves the H₂O and H₂S models, which overtake the null hypothesis line at just before and after 10^{-4} VMR, respectively. We extracted these molecular combinations that present the best χ^2_{red} values, locked the trace molecules to their respective best values, and studied them further. In the lower panel, H₂O is locked at 10^{-6} VMR and we examine the scenario wherein CO₂ is the only atmospheric molecule present. When the CO₂ and H₂S combination was examined, it was seen to be almost precisely the same as the CO₂ model, and thus was omitted to prevent redundancy. Looking further at the lower panel of the plot, the CO₂ and H₂O combination results in the lowest χ^2_{red} value reached in our simulation, approximately 0.83. In comparison, the CO₂ simulation reached a χ^2_{red} minima at 0.93. Both models overtake the null hypothesis just before 10^{-3} , at which point both models become less plausible than the potential of no atmosphere.

Shown in Figure 10 are the retrieved models from the two best sets of abundance values described above in comparison to the L 98-59 c data, with uncertainties. Figure 10 shows that our models fit the observed data well. In particular, the presence of H₂O is necessary for the model to fit the 1.35–1.5 μm wavelength region.

6. Discussion

Herein, we presented HST observations of a single transit of the planet L 98-59 c. Using data from the G141 grism setting for the WFC3 instrument on HST, we extracted a spectrum using our DEFLATE data reduction and analysis software. The final best spectrum (i.e., $\chi^2_{\text{red}} = 0.83$) shows hints of deviations from a featureless spectrum, but the uncertainties on the data are sufficiently large to be fully consistent with a flat featureless spectrum (i.e., $\chi^2_{\text{red}} = 1.14$).

We performed atmospheric modeling with two different parameterized modeling schemes, using the open-source tools PLATON (M. Zhang et al. 2019) and PSG (G. L. Villanueva et al. 2018), to determine limits on composition and cloud-top pressure that would still be consistent with the data.

The current uncertainties on the data are too large to conclusively determine anything beyond upper limits for a cloud-free or a deep-cloud (>1 bar) scenario. However, our analysis with the PLATON Bayesian retrieval code as well as a χ^2_{red} analysis using forward models from PSG are both suggestive of molecular features. The PLATON retrieval finds a best-fit result consistent with an H₂-dominated atmosphere with an elevated metallicity, while the PSG analysis finds that the data are best fit with small contributions from H₂O and CO₂, with VMRs of 5×10^{-6} and 9×10^{-3} , respectively.

6.1. Stellar Activity and Prospects for Stellar Spectral Contamination

L 98-59 was previously assumed to be a quiet star based on the analysis of TESS light curves available at the time the L 98-59 planets were discovered (V. B. Kostov et al. 2019). However, significantly more TESS data have since been collected for this system. We reexamined the TESS 2 minutes cadence data to search for signs of stellar activity. We visually inspected approximately 14 months of TESS time-series data that revealed five flares in the data, shown in Figure 11, of which at least one appears to have multiple peaks, indicative of a complex flare profile.

We modeled these five flares using software we developed, called `xoflares` (T. Barclay & E. Gilbert 2020). This version of the software implements the G. T. Mendoza et al. (2022) flare template. We subsampled the light curves by a factor of 7 to account for the nonlinear changes in brightness occurring during a flare. The software uses a Hamiltonian Monte Carlo method to efficiently sample the flare properties. We found that the peak flare brightness ranged from 0.2% to 3.5%, which are not untypical values for mid-M dwarf stars (R. R. Paudel et al. 2021, 2024).

No rotational variability is visible in the TESS data, but with a rotational period of approximately 80 days (O. D. S. Demangueon et al. 2021) low amplitude variability would be challenging to measure. While rotation modulations in photometric light curves can shed light on the presence and (lower) limits of starspots and faculae, given the flare activity identified it is likely that L 98-59 has some level of surface inhomogeneities because flares are frequently associated with starspots (L. Doyle et al. 2019).

Despite the lack of constraints on rotation modulation—and thus constraints on spot coverage—on L 98-59, we performed an analysis similar to that presented in T. Barclay et al. (2021) to determine whether we could generate a model of stellar contamination that could mimic the transmission spectrum seen in Figure 4. In T. Barclay et al. (2021), HST observations of the planet K2-18 b were reanalyzed to explore whether stellar spectral contamination could be the source (or a contributing factor) of the detected planetary atmospheric signal that was reported in B. Benneke et al. (2019b) and A. Tsiaras et al. (2019). For this exercise, random but plausible stellar spot models were created that emulated the observed photometric spot modulation seen in K2-18 photometric data, and simulations were performed to explore whether the water absorption signal could be a false positive arising from the inhomogeneities on the surface of the star. While the detection of water in the atmosphere of K2-18 b was not ruled out, it was determined that starspots could create the observed signal.

We performed the same exercise for L 98-59, but were not successful—the fairly simple model used in the T. Barclay

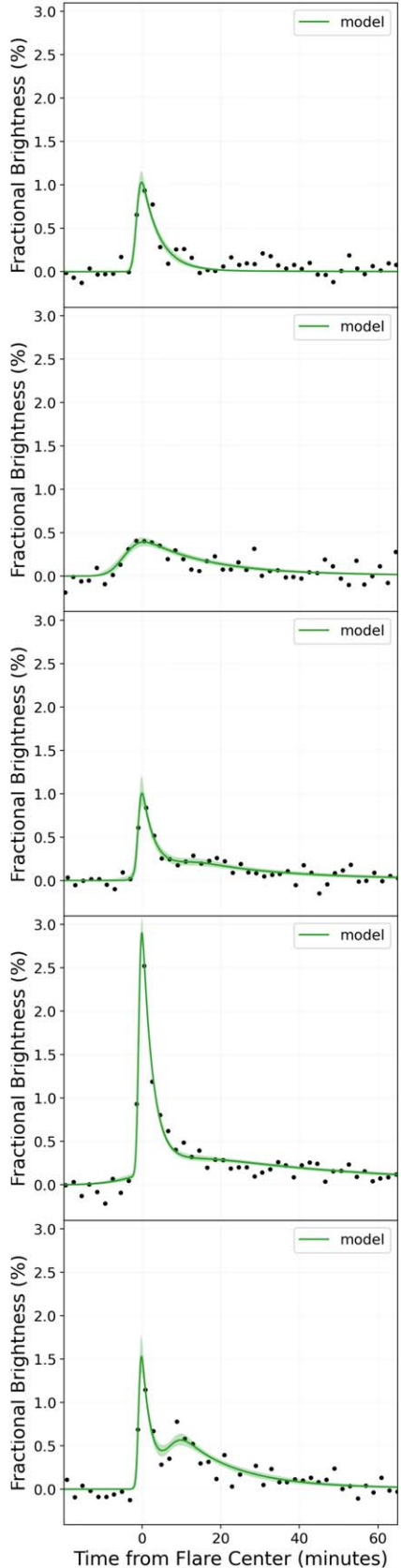


Figure 11. Five flares of L 98-59 seen in TESS 2 minutes cadence data. The flares vary in peak fractional change in stellar brightness from 0.2% to 3.5%. There is also one complex flare that shows multiple peaks. The green curves are flare models with uncertainty regions inferred using an MCMC method.

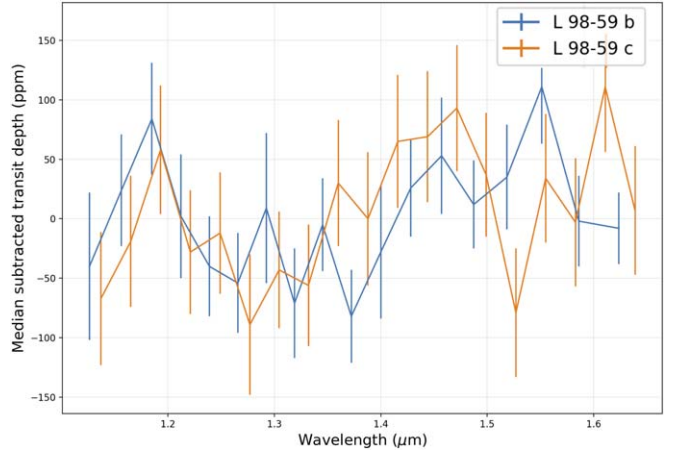


Figure 12. Observations of L 98-59 b and c were taken by HST just 12.5 hr apart. There is correlation between the two observations, which could indicate a common systematic. The L 98-59 b data shown here are from Visit 2 of five, and are the data set most correlated with the HST observations of L 98-59 c.

et al. (2021) analysis was not able to reproduce the shape of the peak around $1.45 \mu\text{m}$ that we see in the data. We could generate a peak at that location but this was always associated with a second broad peak near $1.3 \mu\text{m}$. Moreover, generating a model that has a >100 ppm peak in the WFC3 G141 wavelength range that also had no clear rotational modulation in TESS data was not possible. However, the analysis performed has numerous limitations. We are cautious in saying anything definitive on the possibility that stellar surface inhomogeneities could be corrupting the observed transmission spectrum because of our poor understanding of M-dwarf surfaces and the distribution of the parameters such as spot coverage, size distribution, and spectral energy distributions.

We also examined the HST observed transit of L 98-59 b (M. Damiano et al. 2022) collected on 2020 April 7 (HST Program GO-15856, PI: T. Barclay), just 12.5 hr before the transit we are examining here (see Table 1 for the properties of both planets). Our purpose in looking at these data was that if the L 98-59 c transit shows evidence for contamination, then the transit of planet b is likely to exhibit similar contamination signatures. This transit was the second of five observed for planet b, and showed properties largely consistent with the other four transits. However, using data from M. Damiano et al. (2022), the standard deviation of the Visit 2 transmission spectra data was the highest of all five visits, and the transit depth measured was also the lowest of all the observed transits, albeit at only a significance of $<2\sigma$. Additionally, in the wavelength range between 1.2 and $1.4 \mu\text{m}$ the values computed for Visit 2 are either the lowest or second lowest for each bin. This results in the appearance of an absorption peak around $1.45 \mu\text{m}$ similar to that seen in the L 98-59 c transit. Figure 12 shows the two transmission spectra overlaid with the median subtracted from each. There are similarities in the shape of the two transmission spectra. Both spectra have dips between 1.2 and $1.4 \mu\text{m}$ and both have absorption peaks between 1.4 and $1.5 \mu\text{m}$.

In an effort to quantify whether the Visit 2 data are more similar to our L 98-59 c transit than the other four transits of L 98-59 b observed at different epochs, we calculated the Pearson correlation coefficient between the planet c data and all visits of the planet b data using the `pearsonr` function from `scipy`

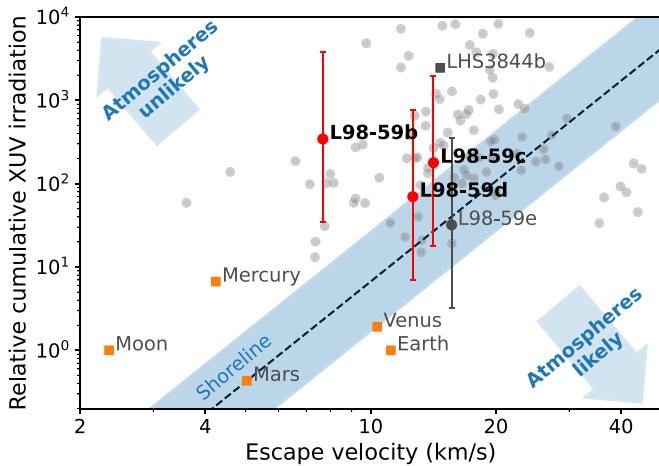


Figure 13. The L 98-59 system provides a unique opportunity to probe the cosmic shoreline. In the solar system, the light blue region separates bodies that have atmospheres from those that do not (K. J. Zahnle & D. C. Catling 2017). Gray dots show known rocky exoplanets with $R < 1.6 R_{\oplus}$ and measured masses and radii. The integrated XUV history of L 98-59 is unknown, so the vertical error bars are representative of M dwarfs (E. L. Shkolnik & T. S. Barman 2014).

(P. Virtanen et al. 2020). Visit 2 was the most correlated with the planet c data, with a probability that the correlation between the data sets occurred by chance of only 13%, while the next highest was Visit 3, at a 47% chance of the correlation occurring by chance. This difference implies that the correlation seen in Visit 2 is 3.6 times less likely to have occurred by random chance than the correlation seen for Visit 3. This is indicative of the Visit 2 data being significantly more correlated than any of the other visits. However, at less than 2σ confidence in this correlation, we are not in a position to say whether the correlation is owing to a common systematic between the two data sets or whether this is simply a coincidence.

6.2. A System of Benchmark Planets

The L 98-59 system provides an excellent opportunity to explore the atmospheres of small planets that evolved in the same stellar environment. The system also provides a unique opportunity to study the “cosmic shoreline” hypothesis (K. J. Zahnle & D. C. Catling 2017), which suggests that there should be a relation between planetary mass and X-ray and ultraviolet (XUV) irradiation that defines a boundary between planets with and without an atmosphere. Although L 98-59 has been previously observed by XMM-Newton, it is challenging to use these data to determine XUV flux because (a) they are missing the UV component, and (b) using single snapshots as a measurement for the integrated XUV flux is biased because flares can occur during observations. So while the integrated XUV history of L 98-59 is not well constrained, using the uncertainties of XUV fluxes representative of M dwarfs (E. L. Shkolnik & T. S. Barman 2014), planets c and d reside near the shoreline (Figure 13; E. S. Kite & M. N. Barnett 2020). If either planet is found to retain an atmosphere, we could place a constraint on the location of the shoreline; alternatively, if the planets are found to be inconsistent with the hypothesis, it would suggest other mass-loss processes (such as impact erosion) are dominant (J. A. Kegerreis et al. 2020).

L 98-59 c and d reside in orbits that, with instellations 4–24 times the insolation that Earth receives from the Sun

(V. B. Kostov et al. 2019; D. Pidhorodetska et al. 2021b), place them within the “Venus zone” (S. R. Kane et al. 2014), a region around a star within which a planet’s atmosphere could potentially be pushed into a runaway greenhouse, producing surface conditions similar to those at Venus. Venus zone planets are highly valuable for comparative planetology efforts that aim to characterize the conditions for planetary habitability (S. R. Kane et al. 2019). While many Venus zone planets have been revealed (C. Ostberg & S. R. Kane 2019; C. Ostberg et al. 2023b), the relatively bright L 98-59 offers a unique opportunity to explore the atmospheres of this class of planets with HST and JWST (D. Pidhorodetska et al. 2021b; C. Ostberg et al. 2023a). The L 98-59 system is thus a benchmark system for examining Venus-class planets that can help place our solar system into context.

7. Conclusions

We observed a single transit of L 98-59 c with Hubble’s WFC3 and find some evidence that the transmission spectrum is not flat, which could be indicative of an exoplanet atmosphere. However, the detection has low significance (2.1σ), therefore our confidence is not sufficiently high to make this a solid claim.

Since the original discovery of the L 98-59 planetary system, more TESS data have been obtained. The star is more active than previously thought, and we observe stellar flares in the star’s light curve. We were not able to simulate any scenarios where stellar spectral contamination could cause the detected signal, although more data will be useful as the spectra of stellar surface inhomogeneities are poorly constrained. We did find some correlation between the transit of L 98-59 b collected just 12.5 hr prior to our L 98-59 c transit. This transit spectrum had the most scatter of any of the five collected, and in the region of wavelength space where contamination is most problematic, this transit spectrum provided a fairly close match to the shape of the L 98-59 c spectrum—there is only 13% chance that the correlation between this transit of planet b and the planet c transit is due to random chance. Moreover, this transit of planet b was much more correlated with the planet c transit than the four other planet b transits that were collected. This correlation is suggestive that both transits suffer from correlated systematics, but not conclusively so as it is at a confidence level of $<2\sigma$.

The single transit of L 98-59 c reported herein limits the conclusions we can draw. A reliable detection will require additional data. Fortunately, L 98-59 c has been selected for additional observations with HST to observe two more transits. As the observations are close to the shot-noise limit, any increase in SNR should scale approximately with the square root of the number of transits observed. Furthermore, observing additional transits provides robustness against a false-positive detection owing to stellar activity.

In addition, observations from JWST (Program 1201, PI: Lafreniere, using the NIRISS instrument in its single-object slitless spectroscopy mode from 0.6 to $2.8 \mu\text{m}$), along with other future HST/JWST data obtained for this star, may shed light on whether the signals presented herein are from stellar spectral contamination or are astrophysical in nature and caused by a planetary atmosphere. If it is the latter, L 98-59 c could be the first planet smaller than 2 Earth radii with a definitively detected atmosphere.

Acknowledgments

This work was supported by the Sellers Exoplanet Environments Collaboration (SEEC) at NASA's Goddard Space Flight Center. This research is based on observations made with the NASA/ESA Hubble Space Telescope obtained from the Space Telescope Science Institute, which is operated by the Association of Universities for Research in Astronomy, Inc., under NASA contract NAS 5-26555. Support for program number HST-GO-15856 was provided through a grant from the STScI under NASA contract NAS5-26555. This paper includes data collected by the TESS mission. Funding for the TESS mission is provided by the NASA's Science Mission Directorate. The material is based upon work supported by NASA under award number 80GSFC21M0002. N. L. gratefully acknowledges support from an NSF GRFP.

Facilities: HST (WFC3), TESS.

Software: Astropy (Astropy Collaboration et al. 2013, 2018), Batman (L. Kreidberg 2015), DEFLATE (K. B. Sheppard et al. 2017), KMPFIT (J. P. Terlouw & M. G. R. Vogelaar 2015), Matplotlib (J. D. Hunter 2007), MC³ (P. Cubillos et al. 2017), NumPy (C. R. Harris et al. 2020), SciPy (P. Virtanen et al. 2020), xoflares (T. Barclay & E. Gilbert 2020).

ORCID iDs

Thomas Barclay [ID](https://orcid.org/0000-0001-7139-2724) <https://orcid.org/0000-0001-7139-2724>
 Natasha Latouf [ID](https://orcid.org/0000-0001-8079-1882) <https://orcid.org/0000-0001-8079-1882>
 Avi M. Mandell [ID](https://orcid.org/0000-0002-8119-3355) <https://orcid.org/0000-0002-8119-3355>
 Elisa V. Quintana [ID](https://orcid.org/0000-0003-1309-2904) <https://orcid.org/0000-0003-1309-2904>
 Emily A. Gilbert [ID](https://orcid.org/0000-0002-0388-8004) <https://orcid.org/0000-0002-0388-8004>
 Geronimo L. Villanueva [ID](https://orcid.org/0000-0002-2662-5776) <https://orcid.org/0000-0002-2662-5776>
 Giada Arney [ID](https://orcid.org/0000-0001-6285-267X) <https://orcid.org/0000-0001-6285-267X>
 Jonathan Brander [ID](https://orcid.org/0000-0002-2072-6541) <https://orcid.org/0000-0002-2072-6541>
 Knicole D. Colón [ID](https://orcid.org/0000-0001-8020-7121) <https://orcid.org/0000-0001-8020-7121>
 Giovanni Covone [ID](https://orcid.org/0000-0002-2553-096X) <https://orcid.org/0000-0002-2553-096X>
 Mario Damiano [ID](https://orcid.org/0000-0002-1830-8260) <https://orcid.org/0000-0002-1830-8260>
 Shawn D. Domagal-Goldman [ID](https://orcid.org/0000-0003-0354-9325) <https://orcid.org/0000-0003-0354-9325>
 Thomas J. Fauchez [ID](https://orcid.org/0000-0002-5967-9631) <https://orcid.org/0000-0002-5967-9631>
 Stefano Fiscale [ID](https://orcid.org/0000-0001-8371-8525) <https://orcid.org/0000-0001-8371-8525>
 Francesco Gallo [ID](https://orcid.org/0000-0002-9138-4788) <https://orcid.org/0000-0002-9138-4788>
 Renyu Hu [ID](https://orcid.org/0000-0002-0388-8004) <https://orcid.org/0000-0002-0388-8004>
 Edwin S. Kite [ID](https://orcid.org/0000-0002-1426-1186) <https://orcid.org/0000-0002-1426-1186>
 Veselin B. Kostov [ID](https://orcid.org/0000-0001-9786-1031) <https://orcid.org/0000-0001-9786-1031>
 Laura Kreidberg [ID](https://orcid.org/0000-0003-0514-1147) <https://orcid.org/0000-0003-0514-1147>
 James Mang [ID](https://orcid.org/0000-0001-5864-9599) <https://orcid.org/0000-0001-5864-9599>
 Caroline V. Morley [ID](https://orcid.org/0000-0002-4404-0456) <https://orcid.org/0000-0002-4404-0456>
 Susan E. Mullally [ID](https://orcid.org/0000-0001-7106-4683) <https://orcid.org/0000-0001-7106-4683>
 Daria Pidhorodetska [ID](https://orcid.org/0000-0001-9771-7953) <https://orcid.org/0000-0001-9771-7953>
 Joshua E. Schlieder [ID](https://orcid.org/0000-0001-5347-7062) <https://orcid.org/0000-0001-5347-7062>
 Laura D. Vega [ID](https://orcid.org/0000-0002-5928-2685) <https://orcid.org/0000-0002-5928-2685>
 Allison Youngblood [ID](https://orcid.org/0000-0002-1176-3391) <https://orcid.org/0000-0002-1176-3391>
 Sebastian Zieba [ID](https://orcid.org/0000-0003-0562-6750) <https://orcid.org/0000-0003-0562-6750>

References

- Apai, D., Rackham, B. V., Giampapa, M. S., et al. 2018, arXiv:1803.08708
 Astropy Collaboration, Price-Whelan, A.M., Sipőcz, B.M., et al. 2018, *AJ*, 156, 123
 Astropy Collaboration, Robitaille, T. P., Tollerud, E. J., et al. 2013, *A&A*, 558, A33
- Barclay, T., & Gilbert, E. 2020, mrtommyb/xoflares, v0.2.1, Zenodo, doi:10.5281/zenodo.4156285
 Barclay, T., Kostov, V. B., Colón, K. D., et al. 2021, *AJ*, 162, 300
 Batalha, N. E., Lewis, N. K., Line, M. R., Valenti, J., & Stevenson, K. 2018, *ApJL*, 856, L34
 Batalha, N. E., Wolfgang, A., Teske, J., et al. 2023, *AJ*, 165, 14
 Benneke, B., Knutson, H. A., Lothringer, J., et al. 2019a, *NatAs*, 3, 813
 Benneke, B., & Seager, S. 2013, *ApJ*, 778, 153
 Benneke, B., Wong, I., Piaulet, C., et al. 2019b, *ApJL*, 887, L14
 Berta, Z. K., Charbonneau, D., Desert, J.-M., et al. 2012, *ApJ*, 747, 35
 Bourrier, V., Ehrenreich, D., King, G., et al. 2017, *A&A*, 597, A26
 Bourrier, V., Dumusque, X., Dorn, C., et al. 2018, *A&A*, 619, A1
 Burt, J. A., Dragomir, D., Mollière, P., et al. 2021, *AJ*, 162, 87
 Castelli, F., & Kurucz, R. L. 2004, arXiv:astro-ph/0405087
 Claret, A., & Bloemen, S. 2011, *A&A*, 529, A75
 Claret, A., Hauschildt, P. H., & Witte, S. 2012, *A&A*, 546, A14
 Cloutier, R., Astudillo-Defru, N., Bonfils, X., et al. 2019, *A&A*, 629, A111
 Crossfield, I. J. M., Dragomir, D., Cowan, N. B., et al. 2020, *ApJL*, 903, L7
 Cubillos, P., Harrington, J., Loredo, T. J., et al. 2017, *AJ*, 153, 3
 Damiano, M., Hu, R., Barclay, T., et al. 2022, *AJ*, 164, 225
 de Wit, J., Wakeford, H. R., Gillon, M., et al. 2016, *Natur*, 537, 69
 de Wit, J., Wakeford, H. R., Lewis, N. K., et al. 2018, *NatAs*, 2, 214
 Demangeon, O. D. S., Zapatero Osorio, M. R., Alibert, Y., et al. 2021, *A&A*, 653, A41
 Deming, D., & Seager, S. 2017, *JGRE*, 122, 53
 Deming, D., Wilkins, A., McCullough, P., et al. 2013, *ApJ*, 774, 95
 Diamond-Lowe, H., Berta-Thompson, Z., Charbonneau, D., Dittmann, J., & Kempton, E. M. R. 2020, *AJ*, 160, 27
 Diamond-Lowe, H., Berta-Thompson, Z., Charbonneau, D., & Kempton, E. M. R. 2018, *AJ*, 156, 42
 Diamond-Lowe, H., Mendonca, J. M., Charbonneau, D., & Buchhave, L. A. 2023, *AJ*, 165, 169
 Doyle, L., Ramsay, G., Doyle, J. G., & Wu, K. 2019, *MNRAS*, 489, 437
 Dragomir, D., Crossfield, I. J. M., Benneke, B., et al. 2020, *ApJL*, 903, L6
 Espinoza, N., Rackham, B. V., Jordán, A., et al. 2019, *MNRAS*, 482, 2065
 Foreman-Mackey, D., Hogg, D. W., Lang, D., & Goodman, J. 2013, *PASP*, 125, 306
 Fortney, J. J., Mordasini, C., Nettelmann, N., et al. 2013, *ApJ*, 775, 80
 Fu, G., Deming, D., Knutson, H., et al. 2017, *ApJL*, 847, L22
 Gao, P., Thorngren, D. P., Lee, E. K. H., et al. 2020, *NatAs*, 4, 951
 Garcia, L. J., Moran, S. E., Rackham, B. V., et al. 2022, *A&A*, 665, A19
 Gennaro, M., et al. 2018, WFC3 Data Handbook v. 4.0 (Baltimore, MD: STScI) https://www.stsci.edu/files/live/sites/www/files/home/hst/documentation/documents/wfc3/wfc3_dhb_v4.pdf
 Gialluca, M. T., Robinson, T. D., Rugheimer, S., & Wunderlich, F. 2021, *PASP*, 133, 054401
 Gibson, N. P. 2014, *MNRAS*, 445, 3401
 Gillon, M., Jehin, E., Lederer, S. M., et al. 2016, *Natur*, 533, 221
 Gillon, M., Triaud, A. H. M. J., Demory, B.-O., et al. 2017, *Natur*, 542, 456
 Gordon, I., Rothman, L., Hargreaves, R., et al. 2022, *JQSRT*, 277, 107949
 Greene, T. P., Bell, T. J., Ducrot, E., et al. 2023, *Natur*, 618, 39
 Guo, X., Crossfield, I. J. M., Dragomir, D., et al. 2020, *AJ*, 159, 239
 Harris, C. R., Millman, K. J., van der Walt, S. J., et al. 2020, *Natur*, 585, 357
 Haynes, K., Mandell, A. M., Madhusudhan, N., Deming, D., & Knutson, H. 2015, *ApJ*, 806, 146
 Hunter, J. D. 2007, *CSE*, 9, 90
 Iyer, A. R., Swain, M. R., Zellem, R. T., et al. 2016, *ApJ*, 823, 109
 Kane, S. R., Arney, G., Crisp, D., et al. 2019, *JGRE*, 124, 2015
 Kane, S. R., Kopparapu, R. K., & Domagal-Goldman, S. D. 2014, *ApJ*, 794, L5
 Kegerreis, J. A., Eke, V. R., Catling, D. C., et al. 2020, *ApJ*, 901, L31
 Keller-Rudek, H., Moortgat, G. K., Sander, R., & Sørensen, R. 2013, *ESSD*, 5, 365
 Kempton, E. M. R., Bean, J. L., Louie, D. R., et al. 2018, *PASP*, 130, 114401
 Kempton, E. M. R., Lupu, R., Owusu-Asare, A., Slough, P., & Cale, B. 2017, *PASP*, 129, 044402
 Kite, E. S., & Barnett, M. N. 2020, *PNAS*, 117, 18264
 Kofman, V., & Villanueva, G. L. 2021, *JQSRT*, 270, 107708
 Kostov, V. B., Schlieder, J. E., Barclay, T., et al. 2019, *AJ*, 158, 32
 Kreidberg, L. 2015, *PASP*, 127, 1161
 Kreidberg, L. 2018, Handbook of Exoplanets (Berlin: Springer), 100
 Kreidberg, L., Bean, J. L., Dsert, J.-M., et al. 2014, *Natur*, 505, 6972
 Kreidberg, L., Koll, D. D. B., Morley, C., et al. 2019, *Natur*, 573, 87
 Kuntschner, H., Bushouse, H., Kümmel, M., & Walsh, J. R. 2009, ST-ECF Instrument Science Report WFC3-2009-17

- Libby-Roberts, J. E., Berta-Thompson, Z. K., Diamond-Lowe, H., et al. 2022, *AJ*, **164**, 59
- Lim, O., Benneke, B., Doyon, R., et al. 2023, *ApJL*, **955**, L22
- Lopez, E. D., & Fortney, J. J. 2014, *ApJ*, **792**, 1
- Lustig-Yaeger, J., Meadows, V. S., & Lincowski, A. P. 2019, *AJ*, **158**, 27
- Mandell, A. M., Haynes, K., Sinukoff, E., et al. 2013, *ApJ*, **779**, 128
- McCullough, P. R., Crouzet, N., Deming, D., & Madhusudhan, N. 2014, *ApJ*, **791**, 55
- Mendoza, G. T., Davenport, J. R. A., Agol, E., Jackman, J. A. G., & Hawley, S. L. 2022, *AJ*, **164**, 17
- Mikal-Evans, T., Madhusudhan, N., Dittmann, J., et al. 2023, *AJ*, **165**, 84
- Moran, S. E., Hörst, S. M., Batalha, N. E., Lewis, N. K., & Wakeford, H. R. 2018, *AJ*, **156**, 252
- Moran, S. E., Stevenson, K. B., Sing, D. K., et al. 2023, *ApJL*, **948**, L11
- Morley, C. V., Kreidberg, L., Rustamkulov, Z., Robinson, T., & Fortney, J. J. 2017, *ApJ*, **850**, 121
- Mugnai, L. V., Modirrousta-Galian, D., Edwards, B., et al. 2021, *AJ*, **161**, 284
- Newton, E. R., Mann, A. W., Kraus, A. L., et al. 2021, *AJ*, **161**, 65
- Nikolov, N., Sing, D. K., Pont, F., et al. 2014, *MNRAS*, **437**, 46
- Ostberg, C., & Kane, S. R. 2019, *AJ*, **158**, 195
- Ostberg, C., Kane, S. R., Li, Z., et al. 2023b, *AJ*, **165**, 168
- Ostberg, C., Kane, S. R., Lincowski, A. P., & Dalba, P. A. 2023a, *AJ*, **166**, 213
- Parmentier, V., & Guillot, T. 2014, *A&A*, **562**, A133
- Paudel, R. R., Barclay, T., Schlieder, J. E., et al. 2021, *ApJ*, **922**, 31
- Paudel, R. R., Barclay, T., Youngblood, A., et al. 2024, *AJ*, **971**, 24
- Pidhorodetska, D., Moran, S. E., Schwieferman, E. W., et al. 2021a, arXiv:2106.00685
- Pidhorodetska, D., Moran, S. E., Schwieferman, E. W., et al. 2021b, *AJ*, **162**, 169
- Pont, F., Knutson, H., Gilliland, R. L., Moutou, C., & Charbonneau, D. 2008, *MNRAS*, **385**, 109
- Pont, F., Sing, D. K., Gibson, N. P., et al. 2013, *MNRAS*, **432**, 2917
- Pont, F., Zucker, S., & Queloz, D. 2006, *MNRAS*, **373**, 231
- Rackham, B., Espinoza, N., Apai, D., et al. 2017, *ApJ*, **834**, 151
- Rackham, B. V., Apai, D., & Giampapa, M. S. 2018, *ApJ*, **853**, 122
- Rackham, B. V., Apai, D., & Giampapa, M. S. 2019a, *AJ*, **157**, 157
- Rackham, B. V., Pinhas, A., Apai, D., et al. 2019b, *BAAS*, **51**, 328
- Ricker, G. R., Winn, J. N., Vanderspek, R., et al. 2015, *JATIS*, **1**, 014003
- Rodgers, C. D. 2000, Inverse Methods for Atmospheric Sounding: Theory and Practice (Singapore: World Scientific)
- Shapiro, S. S., & Wilk, M. B. 1965, *Biometrika*, **52**, 591
- Sheppard, K. B., Mandell, A. M., Tamburo, P., et al. 2017, *ApJL*, **850**, L32
- Sheppard, K. B., Welbanks, L., Mandell, A. M., et al. 2021, *AJ*, **161**, 51
- Shkolnik, E. L., & Barman, T. S. 2014, *AJ*, **148**, 64
- Sing, D. K., Désert, J. M., Fortney, J. J., et al. 2011, *A&A*, **527**, A73
- Skilling, J. 2004, in AIP Conf. Ser. 735, Bayesian Inference and Maximum Entropy Methods In Science and Engineering: 24th Int. Workshop on Bayesian Inference and Maximum Entropy Methods in Science and Engineering, ed. R. Fischer, R. Preuss, & U.V. Toussaint (Melville, NY: AIP), 395
- Speagle, J. S. 2020, *MNRAS*, **493**, 3132
- Swain, M. R., Estrela, R., Roudier, G. M., et al. 2021, *AJ*, **161**, 213
- Terlouw, J. P., & Vogelaar, M. G. R. 2015, Kapteyn Package, v2.3b6 (Groningen: Kapteyn Astronomical Institute) <http://www.astro.rug.nl/software/kapteyn/>
- Trotta, R. 2008, *ConPh*, **49**, 71
- Tsiaras, A., Waldmann, I. P., Rocchetto, M., et al. 2016, *ApJ*, **832**, 202
- Tsiaras, A., Waldmann, I. P., Tinetti, G., Tennyson, J., & Yurchenko, S. N. 2019, *NatAs*, **3**, 1086
- Tsiaras, A., Waldmann, I. P., Zingales, T., et al. 2018, *AJ*, **155**, 156
- Villanueva, G. L., Liuzzi, G., Faggi, S., et al. 2022, Fundamentals of the Planetary Spectrum Generator (Greenbelt, MD: Geronimo)
- Villanueva, G. L., Smith, M. D., Protopapa, S., Faggi, S., & Mandell, A. M. 2018, *JQSRT*, **217**, 86
- Virtanen, P., Gommers, R., Oliphant, T. E., et al. 2020, *NatMe*, **17**, 261
- Wakeford, H. R., Sing, D. K., Evans, T., Deming, D., & Mandell, A. 2016, *ApJ*, **819**, 10
- Wakeford, H. R., Sing, D. K., Deming, D., et al. 2013, *MNRAS*, **435**, 3481
- Wakeford, H. R., Lewis, N. K., Fowler, J., et al. 2019, *AJ*, **157**, 11
- Woitke, P., Helling, C., Hunter, G. H., et al. 2018, *A&A*, **614**, A1
- Zahnle, K. J., & Catling, D. C. 2017, *ApJ*, **843**, 122
- Zhang, M., Chachan, Y., Kempton, E. M. R., & Knutson, H. A. 2019, *PASP*, **131**, 034501
- Zhou, Y., Apai, D., Lew, B. W. P., & Schneider, G. 2017, *AJ*, **153**, 243
- Zieba, S., Kreidberg, L., Ducrot, E., et al. 2023, *Natur*, **620**, 746